

AWARD NUMBER: W81XWH-15-1-0613

TITLE: Fusing MRI and Mechanical Imaging for Improved Prostate Cancer Diagnosis

PRINCIPAL INVESTIGATOR: Dr. Mahdi Orooji

CONTRACTING ORGANIZATION:

Case Western Reserve University
Cleveland, Ohio 44106-7207

REPORT DATE: October 2016

TYPE OF REPORT: Annual

PREPARED FOR: U.S. Army Medical Research and Materiel Command
Fort Detrick, Maryland 21702-5012

DISTRIBUTION STATEMENT: Approved for Public Release;
Distribution Unlimited

The views, opinions and/or findings contained in this report are those of the author(s) and should not be construed as an official Department of the Army position, policy or decision unless so designated by other documentation.

REPORT DOCUMENTATION PAGE

Form Approved
OMB No. 0704-0188

Public reporting burden for this collection of information is estimated to average 1 hour per response, including the time for reviewing instructions, searching existing data sources, gathering and maintaining the data needed, and completing and reviewing this collection of information. Send comments regarding this burden estimate or any other aspect of this collection of information, including suggestions for reducing this burden to Department of Defense, Washington Headquarters Services, Directorate for Information Operations and Reports (0704-0188), 1215 Jefferson Davis Highway, Suite 1204, Arlington, VA 22202-4302. Respondents should be aware that notwithstanding any other provision of law, no person shall be subject to any penalty for failing to comply with a collection of information if it does not display a currently valid OMB control number. **PLEASE DO NOT RETURN YOUR FORM TO THE ABOVE ADDRESS.**

1. REPORT DATE October 2016		2. REPORT TYPE Annual		3. DATES COVERED 15 Sept2015- 14 Sep 2016	
4. TITLE AND SUBTITLE Fusing MRI and Mechanical Imaging for Improved Prostate Cancer				5a. CONTRACT NUMBER	
				5b. GRANT NUMBER W81XWH-15-1-0613	
				5c. PROGRAM ELEMENT NUMBER	
6. AUTHOR(S) Dr. Mahdi Orooji E-Mail:mahdi.orooji@case.edu				5d. PROJECT NUMBER	
				5e. TASK NUMBER	
				5f. WORK UNIT NUMBER	
7. PERFORMING ORGANIZATION NAME(S) AND ADDRESS(ES) Center for Computational Imaging and Personalized Diagnostics the Department of Biomedical Engineering, Western Reserve University 2071 Martin Luther King Drive Cleveland, Ohio 44106-7207				8. PERFORMING ORGANIZATION REPORT NUMBER	
9. SPONSORING / MONITORING AGENCY NAME(S) AND ADDRESS(ES) U.S. Army Medical Research and Materiel Command Fort Detrick, Maryland 21702-5012				10. SPONSOR/MONITOR'S ACRONYM(S)	
				11. SPONSOR/MONITOR'S REPORT NUMBER(S)	
12. DISTRIBUTION / AVAILABILITY STATEMENT Approved for Public Release; Distribution Unlimited					
13. SUPPLEMENTARY NOTES					
14. ABSTRACT The main purpose of this project is to develop computerized fusion algorithms for combining a novel FDA approved imaging modality, prostate mechanical imaging (PMI), with multi-parametric MRI to improve the diagnosis of prostate cancer, especially in the context of repeat biopsies.					
15. SUBJECT TERMS					
16. SECURITY CLASSIFICATION OF:			17. LIMITATION OF ABSTRACT Unclassified	18. NUMBER OF PAGES	19a. NAME OF RESPONSIBLE PERSON USAMRMC
a. REPORT Unclassified	b. ABSTRACT Unclassified	c. THIS PAGE Unclassified			19b. TELEPHONE NUMBER (include area code)

Table of Contents

	<u>Page</u>
1. Introduction.....	4
2. Keywords.....	5
3. Accomplishments.....	6
4. Impact.....	16
5. Changes/Problems.....	17
6. Products.....	18
7. Participants & Other Collaborating Organizations.....	19
8. Special Reporting Requirements.....	20
9. Appendices.....	21

Introduction:

This project serves to address the urgent need for marked improvement in prostate cancer (PCa) detection and diagnosis via the use of multimodal imaging for (a) biopsy planning and guidance, (b) PCa grading and staging, (c) active surveillance, and (d) treatment targeting and monitoring; due to severe limitations with current clinical protocol. For example, in May 2012 the US Preventive Task Force issued a recommendation against PSA based screening for PCa, concluding that it causes more harm than good. Current prostate biopsy procedures which primarily use conventional ultrasound (US) only have an estimated sensitivity of approximately 50%, with 90% of US-guided biopsies being negative. Similarly, focal therapy to treat PCa is gaining interest as a mean of reducing toxic side effects, but it is unlikely to gain favor unless a reliable mean of imaging and subsequently validating presence and extent of PCa is forthcoming.

A novel elastography tool, Prostate Mechanical Imaging (PMI) developed by Artann Labs, is newly FDA approved for PCa screening. Unlike conventional B-mode US, PMI allows for the measurement of gland volume and mechanical stress patterns on the gland surface through the rectal wall with pressure sensor arrays. However, PMI lacks the high spatial resolution of Magnetic Resonance Imaging (MRI). Multi-Parametric MRI (T2W, T1W, Diffusion, and DCE) has recently shown great promise for improving screening and detection of PCa as it provides significant structural and functional parameters for disease characterization. This project is to develop novel computerized fusion methods for precise registration of MRI and PMI in order to enable improved PCa detection in vivo compared to using either PMI or MRI alone. This research will have an impact on development of reliable and practical clinical means of imaging PCa for improved (1) biopsy planning and guidance, (2) grading and prognosis formulation, (3) active surveillance, (4) treatment planning, (5) disease targeting, and (6) treatment monitoring.

Keywords

Prostate Cancer, Radiomics, Magnetic Resonance Imaging, Prostate Mechanical Imaging, Digital Pathology, Computer Tomography Imaging, Intra-tumoral Texture Features, Shape Features, Vascular Features.

Accomplishments

Summary of Progress to Date:

The project has resulted in 3 peer reviewed abstracts, 1 ongoing journal article, and 1 approved patent. We are currently on track to complete all the remaining tasks proposed in this project by the end of the project period. Below, we describe the specific progress performed under each of the original specific aims and also describe the pending tasks for each specific aim.

Milestone supposed to achieve in the 12th month

- Conference such as SPIE Medical Imaging or International Symposium in Biomedical Imaging
 - o Three abstracts were accepted on
 - 1- 24th International Society for Magnetic Resonance Medicine (ISMRM), 7-13 May 2016, Singapore.
 - 2- American Society of Clinical Oncology (ASCO) Annual Meeting, Jun 3-7 2016, Chicago, IL.
 - 3- 102nd Scientific Assembly and Annual Meeting of Radiological Society of North America (RSNA), Nov 27- Dec 3, Chicago, IL.
- A clinical imaging analysis journal such as Journal of Urology.
 - o A journal on evaluating the computer extracted radiomics for discriminating the cancer from benign infection (Specific Aim 2, Task 1,2 and 3) submitted to Nature Scientific Report
 - o A journal paper is in preparation on using the statistical shape model for the prostate segmentation (Specific Aim 1, Task 1)
- Registration techniques to align MRI, PMI, histology.
 - o An algorithm is developed and presented on 24th International Society for Magnetic Resonance Medicine (ISMRM), 7-13 May 2016, Singapore.
- Methods to map cancer extent from histology (ground truth) onto radiology/mechanical imaging data to define signatures on *in vivo* imaging
 - o An algorithm is developed and presented on 24th International Society for Magnetic Resonance Medicine (ISMRM), 7-13 May 2016, Singapore.
- Fusion and integrated visualization of mechanical and multi-parametric imaging data.
 - o American Society of Clinical Oncology (ASCO) Annual Meeting, Jun 3-7 2016, Chicago, IL.
 - o 102nd Scientific Assembly and Annual Meeting of Radiological Society of North America (RSNA), Nov 27- Dec 3, Chicago, IL.
 - o An algorithm is developed and presented on 24th International Society for Magnetic Resonance Medicine (ISMRM), 7-13 May 2016, Singapore.

Research-Specific Major Task 1: Employing co-registration tools to align MP-MRI, PMI, *ex vivo* histologic sections

- **Aim 1-Task 1: Pre-processing of MP-MRI and histology**, Acquisition of multi-protocol *in vivo* MRI prostate data (T2w, DCE, DWI), prostate mechanical imaging data, with corresponding whole-mount histological (WMH) data from our collaborators.

My co-mentor, Dr. Lee Ponsky, Urologist and Professor at the University Hospital Cleveland Medical Center (UHCMC), Case Western Reserve University accepted the primary responsibility to select cases for this project. Besides, Dr. Nicolas Bloch in Boston University School of Medicine, Boston, Massachusetts helped us by providing MRI and ultrasound of the prostate images. To develop the co-registration methodology for MRI-PMI fusion, we employed MRI-TRUS fusion algorithm. Table 1 shows the data we used in MRI-TRUS-WMH fusion.

Table 1: Acquired data for MRI-TRUS-WMH registration

Modality	MRI T1	MRI T2	Transrectal Ultrasound	Whole Mount Histological
Number of Studies	12	15	31	6

The main part of pre-processing of the acquired data was focused on the prostate segmentation in the transrectal ultrasound. PI employed the statistical shape model for the prostate segmentation. A brief description and the results of employed method are as follows. The ongoing paper is attached in the appendices.

- *Using statistical shape model for the prostate segmentation in the transrectal ultrasound image*

An accurate detection of the prostate volume and boundary is influential on diagnosis, treatment, and follow up of CaP. Within this framework, prostate segmentation on TRUS imagery is performed via introduced spatial statistic aware segmentation paradigm. The spatial prior probability is calculated in the training phase, and is used to estimate the texture feature parameters corresponding to the prostate and the background. Estimated parameters is employed to represent an alternative probabilistic presentation of the prostate in TRUS. Results show the 3D prostate capsule is more pronounced in the new representation which ultimately results in more accurate segmentation. Modified active shape model (ASM) is introduced and applied in the new 3D TRUS representation for prostate segmentation. Figure 1 demonstrates the framework of the employed method.

Prostate segmentation in TRUS is a challenging task mainly due to the high inherent noise of the ultrasound images. On the other side, the proficiency of the texture features in the prostate segmentation is already investigated. We employed the power of the texture features in presenting the prostate in the ultrasound images and also the spatial statistics information to introduce an alternative representation. Figure 2 demonstrates the heatmap of the prostate and the background for Haralick features of the TRUS image, in which the prostate capsule is more pronounced in compare to the original TRUS image. We named it the TRUS-HeatMap Representation.

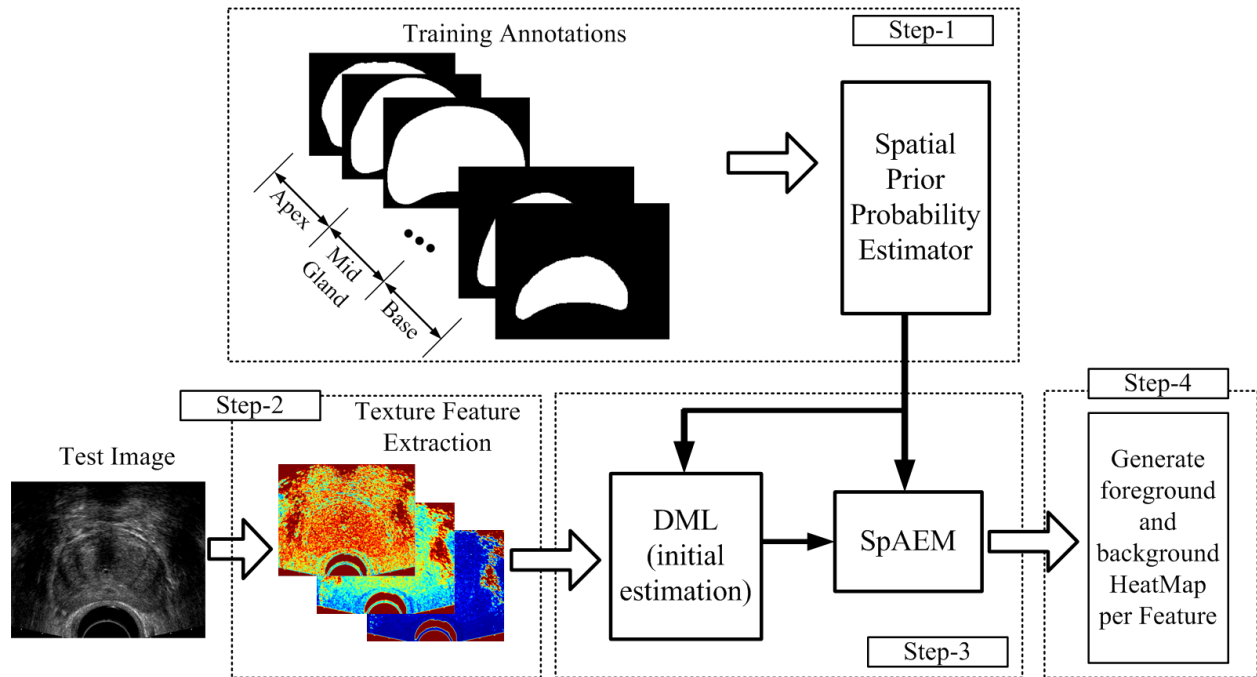


Figure 1: Schematic of four steps used for generating the foreground and background heat-map per texture feature.

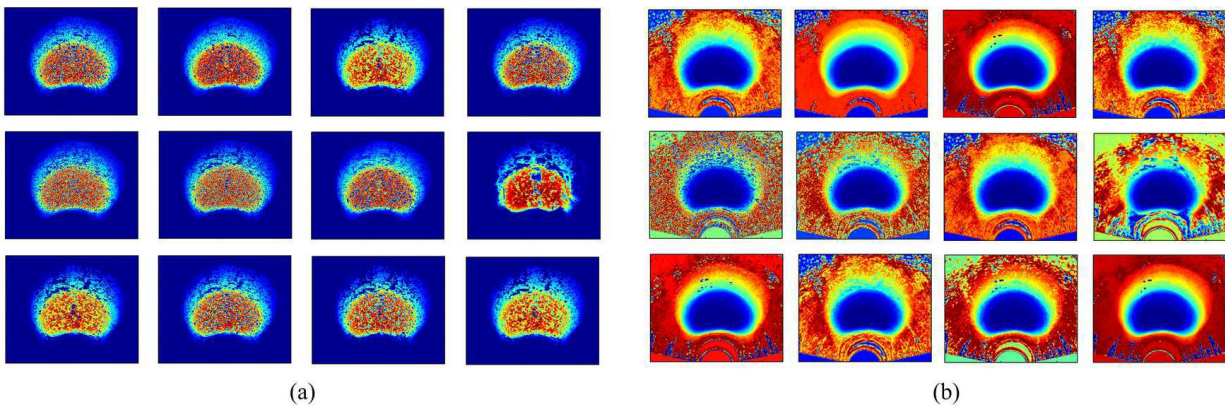


Figure 2. The probability heatmap of (a) the foreground probability and (b) the background probability.

- *Method used for PMI images:*

Prior to each PMI examination the probe is automatically calibrated by placing it into the calibrator. After this, a protective disposable sheath is placed over the PMI transrectal probe including the probe handle. A patient is asked to bend at a 90-degree angle at the hip for the PMI examination. The calibrated PMI probe covered by the sheath is lubricated and gently inserted into the anal canal with sensor surface facing downward. The probe is then gently inserted beyond the anal canal and into rectum until the axial projection of the prostate is visualized on

the computer screen. The prostate scan is performed through a set of multiple manual compressions. The pressure sensor array, in response to input applied pressure, produces a pressure response map on a rectal wall covering the prostate, analogous to that sensed by the physician's finger palpating the prostate during DRE. The PMI provides 3-D pressure mapping of the prostate. This 3-D prostate map/image may be visualized and analyzed after the examination. Figure 3A demonstrates the real time cross-sectional images of the prostate obtained by PMI, and 3B is an actual prostate image of a patient obtained by PMI.

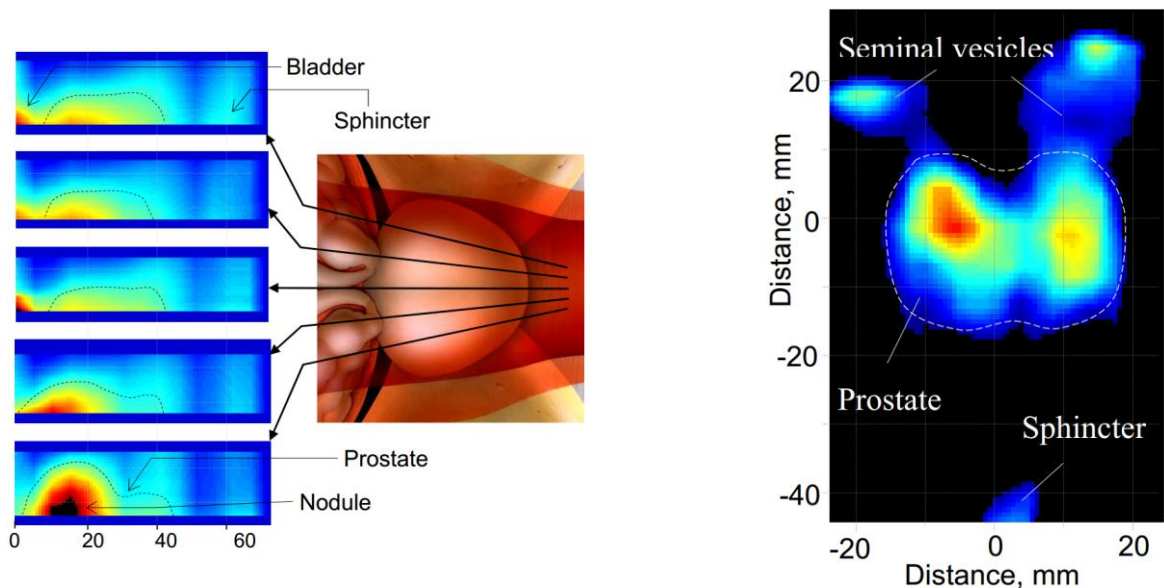


Figure 3. (A) Real time cross-sectional images of the prostate of a patient obtained by 5 successive pressings of the probe over the prostate at different location as shown in the picture. Patient data: PSA - 7.9; DRE - medium size asymmetrical prostate, left sided nodule, firm, immobile. PMI findings: hard nodule located at the prostate base in the left lobe. (B) An example of mechanical image of prostate of a patient.

- **Aim 1, Task 2: Co-registration of PMI with MP-MRI**

Subtask 1: Obtain a segmentation of the prostate on MP-MRI using the methodology Extract a set of features from the PMI capable of distinguishing between prostate tissue and non-prostate tissue.

The ROI was segmented in the previous step. A total of 645 2D texture and 24 3D-shape features were extracted from the segmented area. Texture features were extracted in 2D instead of 3D, since the available retrospective volumes were all anisotropic. After extracting per voxel based features within the nodule of interest, five statistics relating to mean, variance, minimum, maximum and the entropy were calculated. All feature calculations were implemented using MATLAB® 2014b platform (Mathworks, Natick, MA). The description of the extracted texture features and shape features can be found in Table 2 and Table 3.

Table 2: Texture features evaluated in this work.

Feature category	Descriptor	Intuitive Description
<p>Haralick features (Repeated occurrence of grey level configuration in the texture represented via the grey-level co-occurrence matrix (GLCM), which varies rapidly with distance in fine textures and slowly in large textures)</p>	Inverse Difference Moment (IDM)	<p>IDM is a reflection of the presence or absence of uniformity, and hence is a measure of local regions of homogeneity</p> <p>High IDM: Higher presence of locally uniform windows in GLCM</p> <p>Low IDM: Higher presence of locally heterogeneous windows in GLCM</p>
	Correlation	Quantifies the linear patterns in an image based on the distance parameter.
	Sum Entropy	Measure of GLCM relationship to distribution of intensity with respect to entropy. Entropy is the measure of disorder.
	Sum Variance	<p>Measure of GLCM relationship to distribution of intensity with respect to variance</p> <p>High sum variance: greater standard deviation of sum average</p> <p>Low sum variance: low standard deviation of sum average</p>
Laws features	E5, L5, S5, W5, R5 (combination in both X and Y directions)	<p>E- Edges</p> <p>L- Level</p> <p>S- Spots</p> <p>W- Wave</p> <p>R- Ripple</p>
Laplacian pyramids		Multi-resolution filters capture edges at different levels
Gray level features		The basic, intensity based features including mean, median, range and standard deviation.
Gabor Features		Oriented textures via changes in direction and scale; capture microarchitectures
Gradient Features		Represent the directional change in the intensity values of pixels in the ROI
Local Binary Pattern		Thresholding the window with the center pixel value.

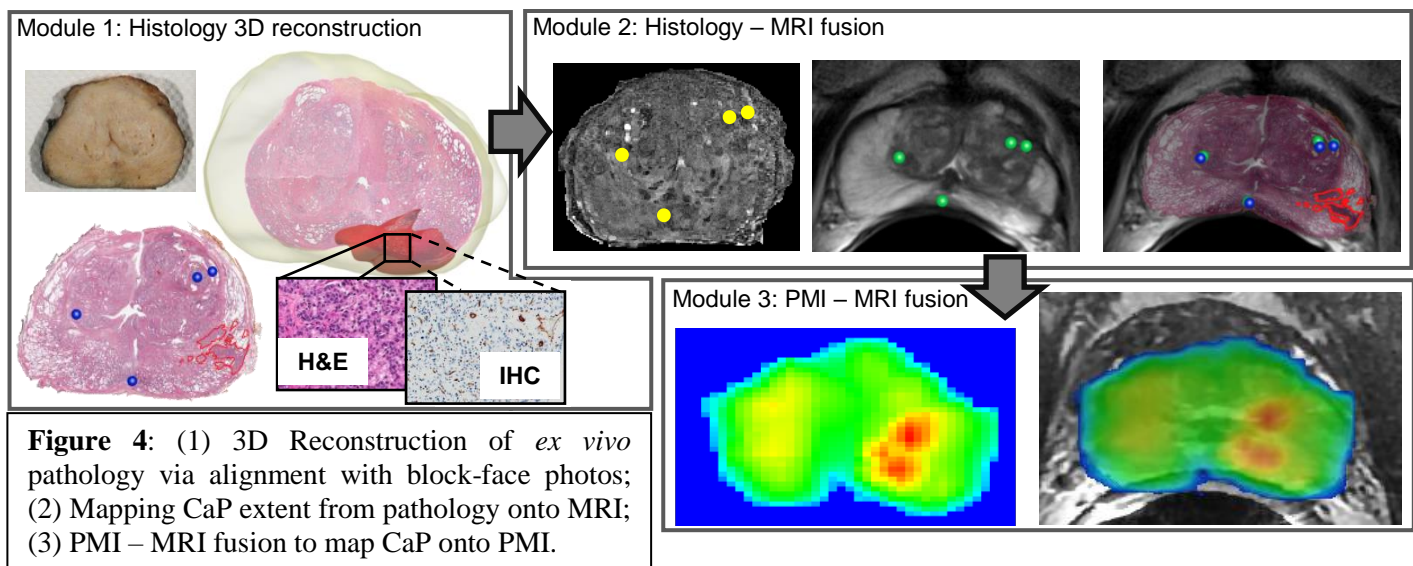
Table 3: Shape features evaluated in this work.

Features	Description
Size	Including Width, Height, Depth of bounding box
Area	from 2D slices of each nodule
Perimeter	from 2D slices of each nodule
Eccentricity	foci of the ellipse and to major axis length
Extend	ratio of pixels in the region to pixels in the total bounding box
Compactness	ratio of the perimeter squared to the product of 4π and area
Radial distance	distances from center of each slice to contour points
Roughness	perimeter of slices divided by convex perimeter
Elongation	from major and minor axis
Convexity	from convex hull
Equivalent Diameter	Diameter of circle with same area of slices
Sphericity	3D compactness

Subtask 2 and 3: Calculate a probabilistic model to estimate the prostate location on PMI and Apply an elastic registration to maximize the overlap between the MP-MRI segmentation and the PMI probabilistic model.

Elastic registration methods developed by the mentor of the PI, at Case Western Reserve University, yield a mapping of prostate cancer extent from *ex vivo* pathology on to corresponding MP-MRI, by allowing for recovery of non-linear deformations between the template and target images. PI extended our previous approaches by inclusion of additional imaging data to facilitate the registration: (1) block face photos of the *ex vivo* pathology, and (2) *ex vivo* MRI of the excised RP. The main steps are:

- Module 1: Reconstruct the 3D volume of the histopathology specimen, Path3D. This was involved (a) aligning the WMH slices to the block face section photos using 2D deformable registration, (2) applying groupwise registration to align block face pictures to each other; (3) implicitly reconstructing the 3D volume and providing a 3D volume for the tumor (see Figure 4).
- Module 2: 3D histology, Path3D, is aligned to the *ex vivo* MRI using 3D deformable co-registration. We then co-registered *ex vivo* to *in vivo* MRI using 3D deformable registration methods, such as finite element modeling (FEM). The transformation was constrained to physically meaningful deformations. Our approach determined optimal deformation forces that maximize similarity metrics based on MRI intensities. This will allow for mapping of CaP annotation from histology on *in vivo* MRI. Figure 4 shows the result of registering WMH (IHC and H&E) to *in vivo* MRI via this technique.



- **Aim 1, Task 3: Evaluating PMI/MP-MRI/Histology registration.**

To provide an optimize tool for MRI/PMI/WMH registration, PI developed MRI/TRUS/WMH registration algorithm. The method was published and presented in the 24th International Society for Magnetic Resonance Medicine (ISMRM), 7-13 May 2016, Singapore. The published abstract and the presented poster is attached in the appendices.

Our study design comprised 12 2D planar images obtained from the MRI and US scans of 3 patients, all of whom had biopsy confirmed prostate cancer and scheduled for a radical prostatectomy. A 3D B-mode ultrasound scan was performed followed by a 3 Tesla MRI prior to surgery. Following surgery and histologic sectioning of the gland via a microtome, the H&E stained whole mount histologic (WMH) sections were digitized via a whole slide scanner and the regions of cancer annotated by an expert pathologist. Deformable co-registration methods were used to spatially align the *in vivo* MRI, TRUS, and *ex vivo* histology. In particular, we used fully automatic Multiattribute probabilistic prostate elastic registration (MAPPER) approach to fusion of ultrasound and MRI. We also manually delineated corresponding landmarks between MRI and WMH for deformable co-registration of WMH to MRI. A total of 129 image features including Haralick, Gabor, Law, LBP, Laplacian features were extracted from both the prostate MRI and TRUS. Each of the computer extracted MRI and ultrasound features were then ranked via the Fisher criteria to identify the features that best identified the region of cancer. Figure 5 illustrates the MRI-TRUS-WMH registration and mapping of the cancer extent on MRI and TRUS.

The top 3 features for each modality and corresponding Fisher criteria values are shown in Table 4. The classification is per region of interest (ROI), i.e. the texture features for the cancerous part of the prostate is compared to the texture features of the noncancerous confounding regions. Top three texture features, contrast variance, contrast entropy, and contrast inverse moment were selected by the theoretical linear discriminant analysis (LDA) classifier for MRI and yielded an area under the receiver operating characteristic curve (AUC) of 0.83, 0.77 and 0.70 for identifying cancerous ROIs in MRI. By comparison, top three most predictive features identified

for TRUS were contrast inverse moment, contrast variance, and contrast entropy. These features yielded an AUC of 0.75, 0.69, and 0.66, respectively. By combining the top two texture features on MRI and the most informative texture feature on TRUS, the LDA based predictor yielded an AUC of 0.88 in predicting presence of prostate cancer. Figure 6 illustrates the scatter plot of the prostate cancer versus the non-cancer cases in three dimensional most informative texture feature space.

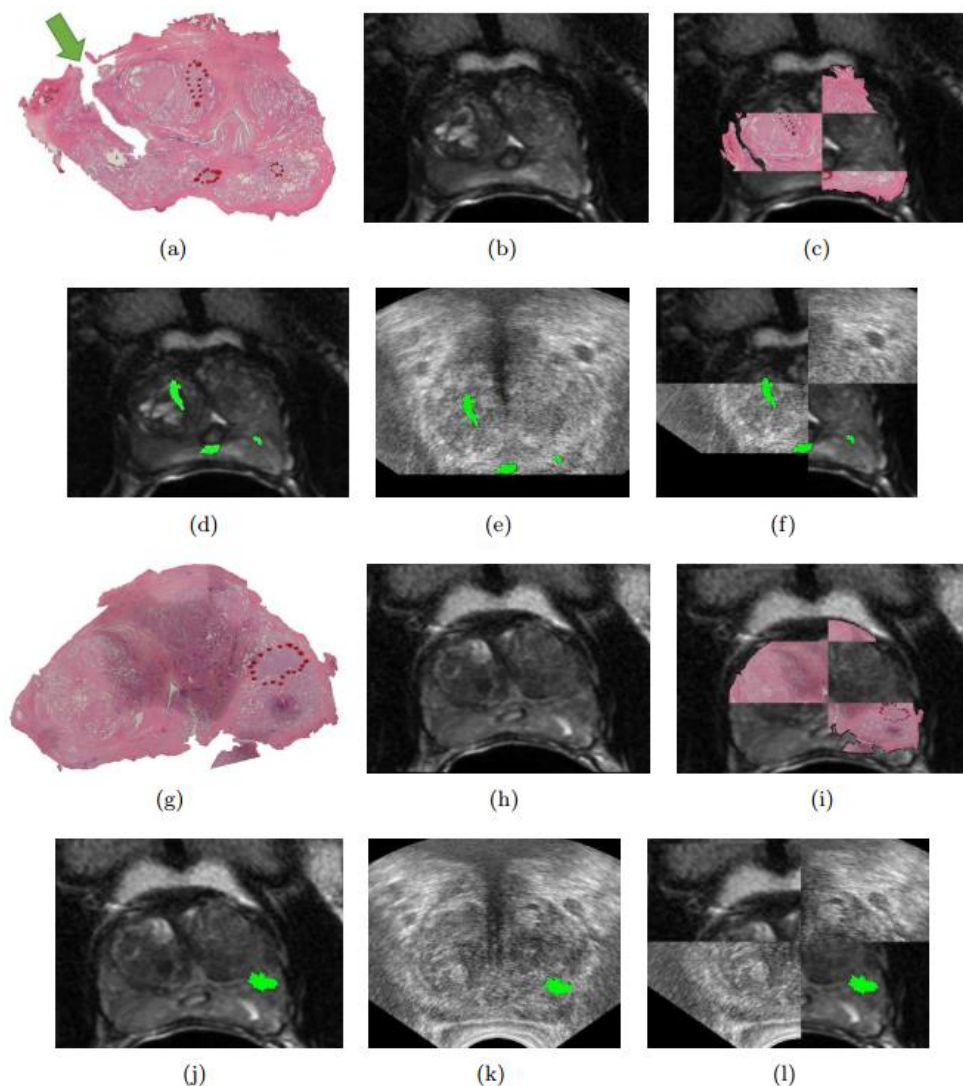


Figure 5: Registration of MRI, TRUS and WMH: Two 2D planar images of (a),(g) WMH and (b),(h) corresponding MRI. (c),(i) WMH and MRI checkerboard overlays showing alignment between the two modalities. (d),(j) MRI with cancer annotation obtained from WMH (green). (e),(k) TRUS with cancer annotation obtained from WMH (green). (f),(l) Fused MRI-TRUS images shown as checkerboards with cancer annotation obtained from WMH (green).

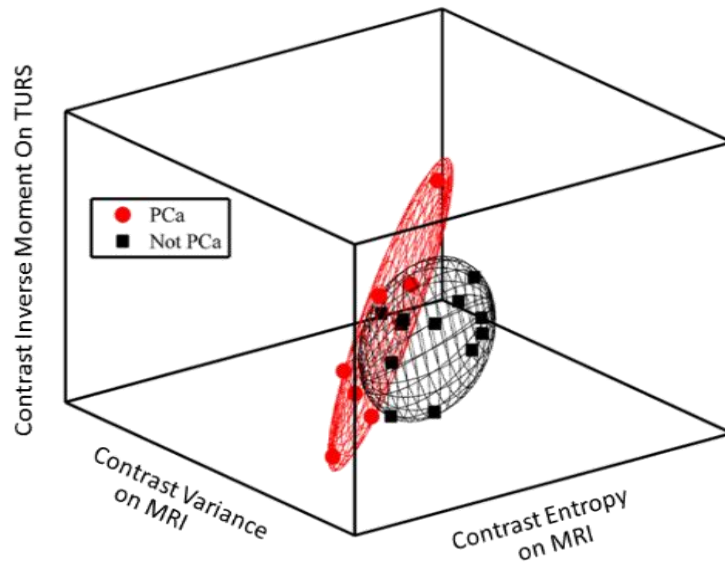


Figure 6: Scatter plot of three most discriminative texture features

Table 4: Top 3 features of MRI and TRUS, and their AUC values

Features for MRI	Contrast Variance	Contrast Entropy	Contrast. Inverse Moment
AUC	0.83	0.77	0.70
Features for TRUS	Contrast. Inverse Moment	Contrast Variance	Contrast Entropy
AUC	0.75	0.69	0.66

Training Specific Aims: Training and educational development in prostate cancer research.

Subtask 1: Mechanical Imaging Training session in Artann Labs (Two weeks in the first year and two weeks in the second year). The PI scheduled the first training session for the middle of December 2016.

Subtask 2: Seminars

- PI had weekly mentor lab meeting, in the Center for Computational Imaging and Personalized Diagnostics (CCIPD) at Case Western Reserve University.
- PI is participating weekly Prostate Imaging Reporting and Data System meeting in the Department of Radiology, Case Medical Center University Hospital with PI’s mentor, clinical co-mentor and radiology collaborators.
- PI is participating the Biomedical Image Analysis Literary Guild (LG) seminar, Case Western Reserve University. Hosted by PI’s mentor.
- PI is participating the majority of Imaging Hour meeting, Department of Biomedical Engineering, Case Western Reserve University.

- PI is participating the majority of monthly Cancer Center Seminar Series, Case Comprehensive Cancer Center.

Subtask 3: Course works

PI studied the course materials of “Cancer Biology, Immunology, and Pathology”, and “Biostatistics”.

Subtask 4: Attending a scientific meeting in relevant scientific field

- PI participated and also presented his works on
 - o American Society of Clinical Oncology (ASCO) Annual Meeting, Jun 3-7 2016, Chicago, IL.
 - o 102nd Scientific Assembly and Annual Meeting of Radiological Society of North America (RSNA), Nov 27- Dec 3, Chicago, IL.

Impact

A novel elastography tool, Prostate Mechanical Imaging (PMI) developed by Artann Labs, is newly FDA approved for PCa screening. Unlike conventional B-mode US, PMI allows for the measurement of gland volume and mechanical stress patterns on the gland surface through the rectal wall with pressure sensor arrays. However, PMI lacks the high spatial resolution of Magnetic Resonance Imaging (MRI). Multi-Parametric MRI (T2W, T1W, Diffusion, and DCE) has recently shown great promise for improving screening and detection of PCa as it provides significant structural and functional parameters for disease characterization. This project developed novel computerized fusion methods for precise registration of MRI and PMI in order to enable improved PCa detection *in vivo* compared to using either PMI or MRI alone. This research have an impact on development of reliable and practical clinical means of imaging PCa for improved (1) biopsy planning and guidance, (2) grading and prognosis formulation, (3) active surveillance, (4) treatment planning, (5) disease targeting, and (6) treatment monitoring.

Changes/Problems

Nothing to report

Products

Accepted and presented abstracts:

- Mahdi Orooji, Mehdi Alilou, Rachel Sparks, Mirabela Rusu, B Nicolas Bloch, Ernest Feleppa, Dean Barratt, Lee Ponsky, Anant Madabhushi, "A Combination of Radiomic Features from MRI and Ultrasound Appears to better predict presence of prostate cancer: Validation against whole mount pathology", 24th International Society for Magnetic Resonance Medicine (ISMRM), 7-13 May 2016, Singapore.
- Orooji, M., Rakshit, S., Beig, N., Velcheti, V., Madabhushi, A., "Computerized textural analysis of lung CT enables quantification of tumor infiltrating lymphocytes in NSCLC", American Society for Clinical Oncology (ASCO) Annual Meeting, Chicago, IL, 2016
- Rakshit, S., Orooji, M., Beig, N., Velcheti, V., Madabhushi, A., "Use of radiomic features on baseline CT scan to predict clinical benefit for pemetrexed based chemotherapy in metastatic lung adenocarcinoma", American Society for Clinical Oncology (ASCO) Annual Meeting, Chicago, IL, 2016
- Mahdi Orooji, Mehdi Alilou, Niha Beig, Sagar Rakshit, Prabhakar Rajiah, Michael Yang, Frank Jacono, Robert Gilkeson, Philip Linden, Vamsidhar Velcheti, Anant Madabhushi, "A combination of shape and texture features enables discrimination of benign fungal infection from non-small cell lung adenocarcinoma on chest CT", 102nd Scientific Assembly and Annual Meeting of Radiological Society of North America (RSNA), Nov 27- Dec 3, Chicago, IL.

Ongoing Journal Article:

- Mahdi Orooji, Mehdi Alilou, Lee Ponsky, Anant Madabhushi, "Spatial Statistic Aware Segmentation Paradigm: Application on the Prostate Segmentation in the Transrectal Ultrasound Images", is going to submit to IEEE Transaction on Medical Imaging.

US Patent

- Madabhushi, Anant (Shaker Heights, OH, US), Rusu, Mirabela (Cleveland, OH, US), Orooji, Mahdi (Cleveland, OH, US), Alilou, Mehdi (Cleveland, OH, US), "Textural Analysis of Lung Nodules", United States Patent Application 20160155225.

Participants & Other Collaborating Organizations.

- What individuals have worked on the project?
 - PI: Mahdi Orooji, PhD: No change
 - Mentor: Anant Madabhushi, PhD: No change
 - Co-mentor: Lee Ponsky, MD: No change
 - Collaborator: Pingfu Fu, PhD: No change
 - Collaborator: Vikas Gulani, MD: No change
 - Collaborator: Raj Paspulati, MD: No Change
 - Collaborator: Armen Sarvazian, PhD: No change
 - Collaborator: Gregory MacLennan, MD: No change
- Has there been a change in the active other support of the PD/PI(s) or senior/key personnel since the last reporting period?
 - Nothing to Report
- What other organizations were involved as partners?
 - Nothing to Report

Special Reporting Requirements

Nothing to report

Appendices

Part 1: Accepted Papers

Abstract #171681

Computerized textural analysis of lung CT to enable quantification of tumor infiltrating lymphocytes in NSCLC.

Mahdi Orooji, Sagar Rakshit, Niha Beig, Anant Madabhushi, Vamsidhar Velcheti; Biomedical Engineering, Case Western Reserve University, Cleveland, OH; Cleveland Clinic Foundation, Cleveland, OH; Case Western Reserve University, Cleveland, OH; Cleveland Clinic, Cleveland, OH

Abstract Text:

Background: Tumor infiltrating lymphocytes (TILs) are a part of the dynamic immune microenvironment. Clinical trials with immune checkpoint inhibitors report significant increase in TILs in responders in follow up tumor biopsies. Monitoring TILs on treatment using radiomic features extracted from routine follow up computed tomographic (CT) images can be a non-invasive surrogate to biopsy to detect early response. We conducted a proof of concept study to find out if radiomic features extracted from CT images can identify patients with high and low TILs in non-small cell lung cancer (NSCLC).

Methods: A cohort of 50 consecutive patients who underwent lobectomy for early stage NSCLC were identified and TIL were characterized using routine hematoxylin and eosin (H&Es) slides. TILs were quantified on a previously reported scale of 0 to 3 based on intensity of TIL. Of the 50 cases 17 outliers who had high TILs (3+) or low TILs (0) were identified. The study team was provided with CT images from 4 patients with '0' TILs, 8 tumors with '3+' TILs and 5 tumors were blinded. Corresponding pre-surgical CT scans were annotated on slicer-3D software. A total of 669 radiomic (textural and shape) features of the lung nodule were investigated. These features were evaluated and ranked in their ability to discriminate TIL extent using a linear discriminant classifier, both in terms of univariate and multivariate analysis.

Results: Sphericity, a shape based feature was the most discriminating feature. Standard deviation and Laws were ranked as the most promising texture based features. Of the 5 blinded tumors, 4 were classified correctly leaving only one misclassified case.

Conclusions: Computerized textural analysis using shape and texture features extracted from the lung nodule on CT images could be used to identify tumors with high TILs. Further validation of these findings in larger independent cohorts is required. These novel imaging based biomarkers could be a useful diagnostic tool for predicting response and monitoring patients on immunotherapy.

Abstract #171139

Evaluation of radiomic features on baseline CT scan to predict clinical benefit for pemetrexed based chemotherapy in metastatic lung adenocarcinoma.

Sagar Rakshit, Mahdi Orooji, Niha Beig, Mehdi Alilou, Nathan A. Pennell, James Stevenson, Marc A. Shapiro, Anant Madabhushi, Vamsidhar Velcheti; Cleveland Clinic Foundation, Cleveland, OH; Biomedical Engineering, Case Western Reserve University, Cleveland, OH; Cleveland Clinic, Cleveland, OH; Case Western Reserve University, Cleveland, OH

Abstract Text:

Background: Many patients receiving standard of care pemetrexed based platinum doublet followed by maintenance pemetrexed for lung adenocarcinoma do not receive clinical benefit. Currently there are no clinically validated biomarkers to identify patients who benefit from these treatments. We conducted a retrospective proof-of concept study to identify predictive computer extracted image features from pre-treatment computed tomographic (CT) scans.

Methods: Pre-chemotherapy CT scans were obtained for 105 lung adenocarcinoma patients treated with pemetrexed based chemotherapy at the Cleveland Clinic from 2004-2010. Clinical benefit was defined as patients with an objective response or more than 12 cycles of pemetrexed therapy. We identified and annotated CT images in 2 groups- 46 with clinical benefit and 59 without clinical benefit. After adjusting for image quality and CT filters, 32 and 33 patients remained for final analysis in the 2 groups respectively. A total of 1108 radiomic features including both textural and shape features of the lung nodule as well as the peritumoral region were investigated. The features were evaluated and ranked in their ability to discriminate between the 2 groups in conjunction with a linear discriminant classifier, both in terms of univariate and multivariate analysis.

Results: Two of the top 3 ranked features were from within the nodule and the third was from within the peritumoral area. Mean of Sum Average, a co-occurrence based texture measure within the nodule was the most discriminating feature. Combination of features within and around the nodule yielded even higher AUC values (See Table for combination of best features).

Conclusions: Texture and shape features extracted from within and around the lung nodule on CT images could identify patients who could potentially benefit from pemetrexed based chemotherapy. Further validation in a larger retrospective, multi-institutional cohort is needed.

Feature Vector	Area Under ROC Curve \pm Standard Deviation
Mean of Intratumoral Sum Average(1)	69.5% \pm 3.0%
1+Minimum of Intratumoral Law L5xE5(2)	75.2% \pm 3.2%
1+2+Mean of Peritumoral Law S5xW5(3)	77.6% \pm 1.9%

A Combination of Radiomic Features from MRI and Ultrasound Appears to better predict presence of prostate cancer: Validation against whole mount pathology

Authors: Mahdi Orooji¹, Mehdi Alilou¹, Rachel Sparks², Mirabela Rusu¹, B Nicolas Bloch³, Ernest Feleppa⁴, Dean Barratt², Lee Ponsky⁵, Anant Madabhushi¹

¹ **Center for Computational Imaging and Personalized Diagnostics, Case Western Reserve University, Cleveland, OH, USA**

²**Centre for Medical Image Computing, University College of London**

³**Boston University School of Medicine, Boston, Massachusetts**

⁴**Lizzi Center for Biomedical Engineering, Riverside Research**

⁵University Hospital Case Medical Center, Case Western Reserve University, Cleveland, OH, USA

Synopsis:

To evaluate whether the combination of computer extracted or radiomic image parameters from two complementary modalities, MRI-Transrectal Ultrasound (TRUS) can enable better prediction of presence of prostate cancer compared to either modality individually. In order to evaluate the ability of the radiomic features from MRI and ultrasound and the combination of MRI and ultrasound radiomic features in predicting the presence of prostate cancer we considered 3 patients who underwent MRI, transrectal ultrasound prior to radical prostatectomy. Deformable co-registration methods were used for spatially aligning the pre-operative *in vivo* MRI and ultrasound with the *ex vivo* whole mount radical prostatectomy specimens to establish the “ground truth” for cancer extent on the imaging. A combination of texture features from US and MRI yielded the best separability between cancer and non-cancer regions with an Area under the operating characteristic curve of 0.88.

PURPOSE:

Recently there has been a great deal of interest in developing computer aided diagnosis systems for identifying prostate cancer presence *in vivo* on MRI and ultrasound

separately¹⁻³, no work we are aware of has attempted to address the issue of fusing computer derived features from MRI and ultrasound to create the best possible predictor of cancer in vivo. In this work we attempt a systematic and quantitative evaluation of the discriminability of computer extracted MRI and ultrasound features in terms of cancer detection in patients undergoing radical prostatectomy.

METHODS:

Our study design comprised 12 2D planar images obtained from the MRI and US scans of 3 patients, all of whom had biopsy confirmed prostate cancer and scheduled for a radical prostatectomy. A 3D B-mode ultrasound scan was performed followed by a 3 Tesla MRI prior to surgery. Following surgery and histologic sectioning of the gland via a microtome, the H&E stained whole mount histologic (WMH) sections were digitized via a whole slide scanner and the regions of cancer annotated by an expert pathologist. Deformable co-registration methods were used to spatially align the in vivo MRI, TRUS, and *ex vivo* histology. In particular, we used fully automatic Multiattribute probabilistic prostate elastic registration (MAPPER) approach to fusion of ultrasound and MRI⁴. We also manually delineated corresponding landmarks between MRI and WMH for deformable co-registration of WMH to MRI. A total of 129 computer extracted image features including Haralick, Gabor, Law, LBP, Laplacian features were extracted from both the prostate MRI and TRUS. Each of the computer extracted MRI and ultrasound features were then ranked via the Fisher criteria to identify the features that best identified the region of cancer. Figure 1 illustrates the MRI-TRUS-WMH registration and mapping of the cancer extent on MRI and TRUS.

RESULTS AND DISCUSSION

The top 3 features for each modality and corresponding Fisher criteria values are shown in Table.1. The classification is per region of interest (ROI), i.e. the texture features for the cancerous part of the prostate is compared to the texture features of the noncancerous confounding regions. Top three texture features, contrast variance, contrast entropy, and contrast inverse moment were selected by the theoretical linear discriminant analysis (LDA) classifier for MRI and yielded an area under the receiver operating characteristic curve (AUC) of 0.83, 0.77 and 0.70

for identifying cancerous ROIs in MRI. By comparison, top three most predictive features identified for TRUS were contrast inverse moment, contrast variance, and contrast entropy. These features yielded an AUC of 0.75, 0.69, and 0.66, respectively. By combining the top two texture features on MRI and the most informative texture feature on TRUS, the LDA based predictor yielded an AUC of 0.88 in predicting presence of prostate cancer. Figure 2 illustrates the scatter plot of the prostate cancer versus the non-cancer cases in three dimensional most informative texture feature space.

CONCLUSION:

We presented a framework to rank the performance of computer extracted MRI and ultrasound features in terms of their ability to identify prostate cancer. Our results in a small cohort suggests that we may be able to combine the MRI and ultrasound radiomic features to create a better classifier for prostate cancer detection compared to MRI or ultrasound alone.

References:

- ¹Emilie Niaf, Olivier Rouvire, Florence Mge-Lechevallier, Flavie Bratan, Carole Lartizien,” Computer-aided diagnosis of prostate cancer in the peripheral zone using multiparametric MRI”, *Physics in Medicine and Biology* 2012.
- ²Tiwari P, Kurhanewicz J, Rosen M, Madabhushi A. (2010) Semi supervised multi kernel (SeSMiK) graph embedding: identifying aggressive prostate cancer via magnetic resonance imaging and spectroscopy. *Med Image Comput Comput Assist Interv.* 13(Pt 3):666-73
- ³Mehdi Moradi, Parvin Mousavi, Purang Abolmaesumi, Computer-Aided Diagnosis of Prostate Cancer with Emphasis on Ultrasound-Based Approaches: A Review, *Ultrasound in Medicine & Biology*, Volume 33, Issue 7, July 2007, Pages 1010-1028, ISSN 0301-5629
- ⁴ Sparks, Rachel and Nicolas Bloch, B. and Feleppa, Ernest and Barratt, Dean and Moses, Daniel and Ponsky, Lee and Madabhushi, Anant, “Multiattribute probabilistic prostate elastic registration (MAPPER): Application to fusion of ultrasound and magnetic resonance imaging”, *Medical Physics*, 42, 1153-1163 (2015),

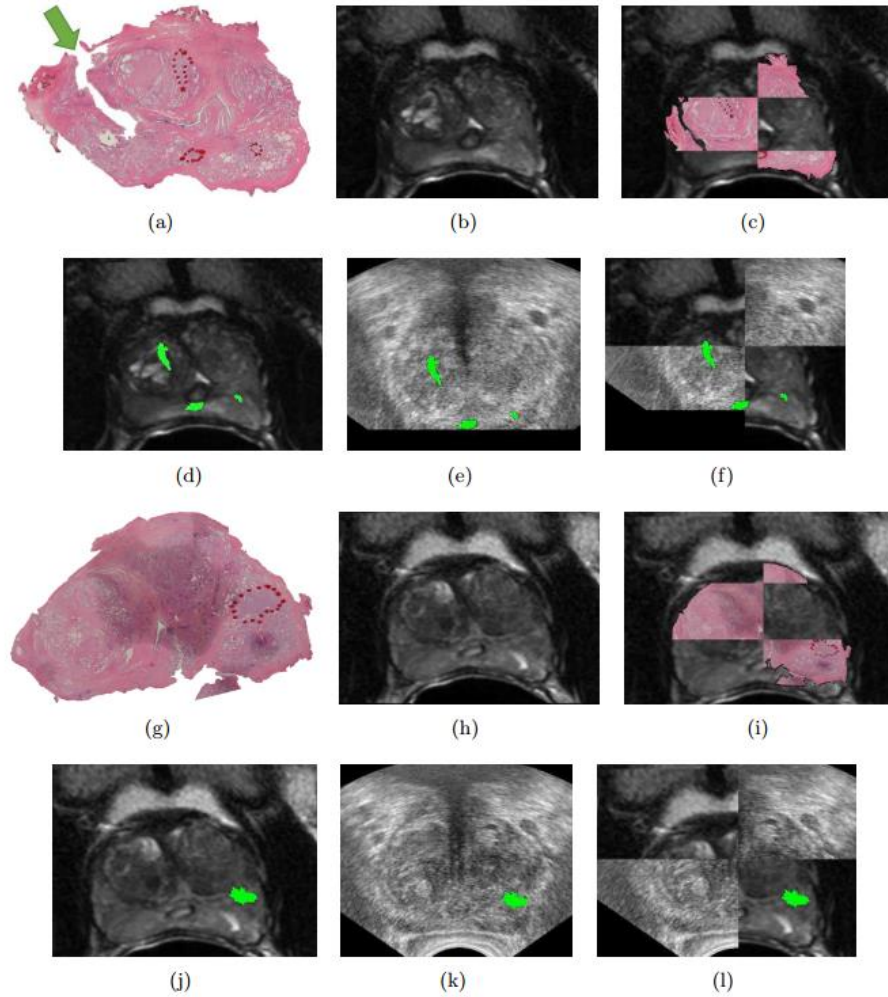


Figure 1: Registration of MRI, TRUS and WMH: Two 2D planar images of **(a),(g)** WMH and **(b),(h)** corresponding MRI. **(c),(i)** WMH and MRI checkerboard overlays showing alignment between the two modalities. **(d),(j)** MRI with cancer annotation obtained from WMH (green). **(e),(k)** TRUS with cancer annotation obtained from WMH (green). **(f),(l)** Fused MRI-TRUS images shown as checkerboards with cancer annotation obtained from WMH (green).

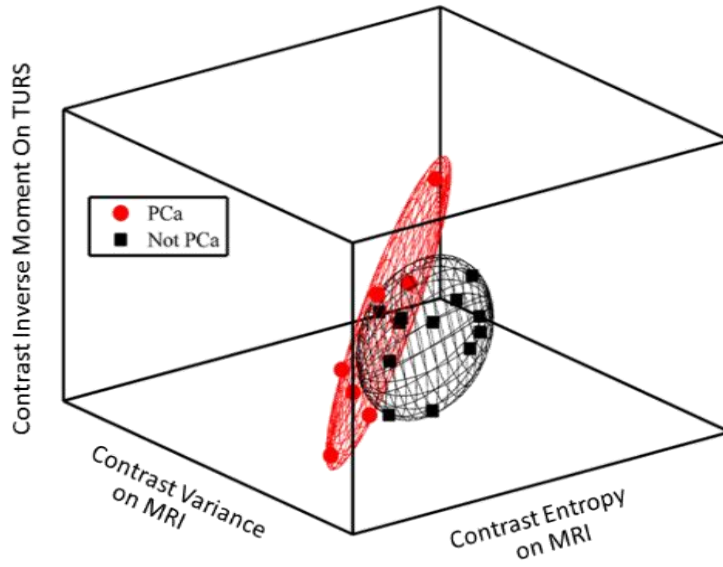


Figure 2: Scatter plot of three most discriminative texture features

Table 1: Top 3 features of MRI and TRUS, and their AUC values

AUC	0.83	Entropy	Inverse Moment
Features for TRUS	Contrast. Inverse Moment	Contrast Variance	Contrast Entropy
AUC	0.75	0.69	0.66

Radiomic Features on Baseline Non-Contrast CT Predict Clinical Benefit for Pemetrexed Based Chemotherapy in Metastatic Lung Adenocarcinoma



Cancer for Computational Models and Personalized Diagnostics

Sagar Rakshit¹, Mahdi Orooji², Niha Baig², Mehdi Aliouf², Nathan A. Pennell¹, James Stevenson¹, Marc A. Shapiro¹, Prabakar Rajiah³, Anant Madabhushi², Vamsidhar Velcheti¹

¹Cleveland Clinic Foundation, Cleveland, OH, USA ²Case Western Reserve University, OH, USA ³University of Texas Southwestern Medical Center, TX, USA



Introduction

Objective
To determine if computer extracted shape and texture features from within the nodule and the peritumoral zone on computerized tomographic (CT) scans can predict benefit and treatment response to pemetrexed based chemotherapy in pulmonary adenocarcinoma.

Background

- Pemetrexed based platinum doublet followed by maintenance pemetrexed for lung adenocarcinoma is the standard of care for patients with no actionable mutations. However many patients receiving such cytotoxic chemotherapy do not receive clinical benefit.
- Response rate to pemetrexed based regimens as initial treatment is around 24-31% while the disease control rate is around 60%(1-2).
- Currently there are no clinically validated biomarkers to identify patients who benefit from these treatments.

Related work and novel contribution

- Textural analysis to predict response to chemotherapy has been done predominantly on pre-treatment DCE-MRI and PET images(3-5).
- Ravanelli et al used pre-treatment CT images to predict response to first line chemotherapy in NSCLC (6).
- In this work we evaluate the predictive benefit of radiomic texture and shape features both within the peritumoral and tumoral compartments. Contributions are:
 - Evaluate role of intra-tumoral texture and lesion shape in predicting response to Chemo.
 - Evaluate role of peritumoral morphology (via textural analysis) in predicting response to Chemo.
 - Evaluate whether combination of intra-tumoral and peri-tumoral features is more predictive of Chemo response

Methodology

Step 1
Dataset curation: CT scans of patients who derived benefit and no benefit from pemetrexed based chemotherapy
Benefit: Objective response or >=12 cycles of pemetrexed

Step 2

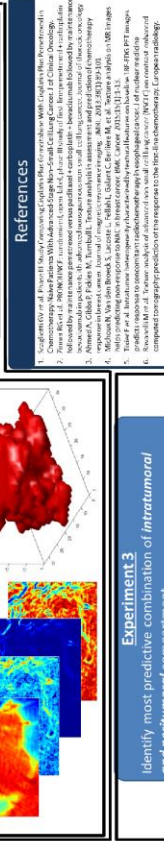
- Annotation of ROI to delineate tumoral and peritumoral volume
- Peritumoral volume defined as the volume between tumor boundary and 7 pixels away. Distance heuristically determined.

Step 3

- Extracting shape and texture feature from the intra and peritumoral compartment of annotated nodule from previous step
- 1108 radiomic descriptors were extracted

Experiment 1
Identify most predictive shape and texture features from the intratumoral compartment

Experiment 2
Identify most predictive shape and texture features from the peritumoral compartment



References

1. Sagar Rakshit et al. Predicting Response to Pemetrexed Based Chemotherapy in Lung Adenocarcinoma Using Radiomic Features on Baseline Non-Contrast CT Scans. *Journal of Thoracic Imaging*, 2020.
2. James Baig et al. Radiomic Features on Baseline Non-Contrast CT Scans Predict Response to Pemetrexed Based Chemotherapy in Lung Adenocarcinoma. *Journal of Thoracic Imaging*, 2020.
3. Ahmed, Ghazi P, Fidler, M, Tumbull, T. Radiomics in cancer diagnosis and prognosis: computational approaches to extract, analyze and combine imaging data. *Journal of Cellular Biochemistry*, 2017.
4. Michonik, V, Jans, B, Scahill, S, Goh, C, Bertram, R, et al. Response to first-line platinum-based chemotherapy in non-small-cell lung cancer: a radiomic study. *Journal of Thoracic Imaging*, 2019.
5. Tardif, J, et al. Radiomic features on baseline PET/CT scans predict response to pemetrexed-based chemotherapy in lung adenocarcinoma. *Journal of Thoracic Imaging*, 2020.
6. Ravanelli, M, et al. Radiomic features on baseline CT scans predict response to first-line chemotherapy in non-small cell lung cancer. *Journal of Thoracic Imaging*, 2020.

Dataset

- Pre-treatment CT scans of N=65 patients treated with pemetrexed chemotherapy at Cleveland Clinic, 32 with and 33 without clinical benefit.
- Lesions were annotated by an expert reader on 3D slicer software

Method

- Feature selection strategy: Features are ranked based on the AUC values and Feed Forward feature selection.
- Linear Discriminant Analysis (LDA) classifier used for prediction. 4-fold cross validation was used for classifier optimization and evaluation.

Experimental results

- Experiment 1:** Mean of intratumoral sum average, the minimum of intratumoral Law L5x65 and Sphericity are the most predictive radiomics, with AUC equals 69.5%, 67.2% and 64.1%, respectively.
- Experiment 2:** Mean of Peritumoral Law S5xW5 is the most informative texture feature with AUC=0.649.
- Experiment 3:** A combination of intratumoral and peritumoral radiomics achieve better prediction accuracy compared to either alone.
- Two of the top 3 ranked features were intratumoral, one was peritumoral.

Feature Category	Feature Vector	AUC
Intratumoral	Mean of Intratumoral Sum Average	69.5% ± 3.2%
	Minimum of Intratumoral Law L5x65	67.2% ± 4.9%
	Sphericity	64.1% ± 3.7%
Peritumoral	Mean of Peritumoral Law S5xW5	64%±48.1%
Intratumoral+ Peritumoral	Mean of Intratumoral Sum Average+ Minimum of Intratumoral Law L5x65+Mean of Peritumoral Law S5xW5	77.6% ± 1.9%

Table 1: Top performing radiomic features and AUC

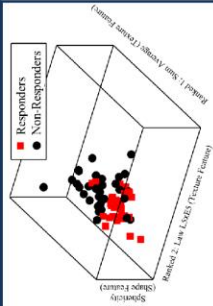


Figure 1: Scatter plot of the most informative intratumoral feature

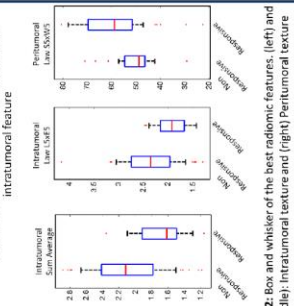


Figure 2: Box and whisker of the best radiomic features, (left) and (middle): Intratumoral texture and (right) Peritumoral texture

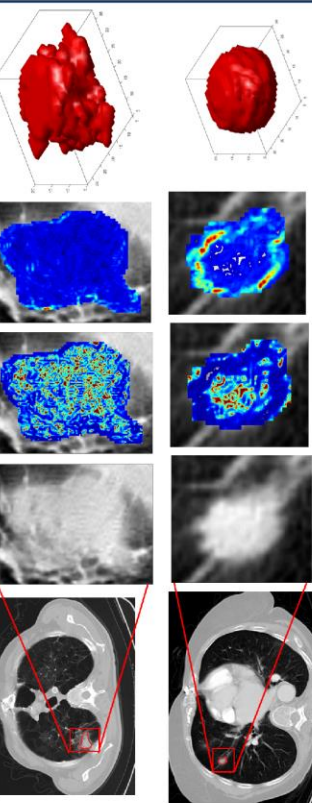


Figure 3: Qualitative demonstration of predictive intra- and peri-tumoral radiomics identified on: (Top Row) Non-Responder and (Bottom Row) Responder. From left to right: Original CT, annotated nodule, Energy texture feature, Difference variance texture feature, sphericity shape feature

Concluding Remarks

- Our analysis highlights the impressive potential of non-invasive and cost-effective radiomics for precision medicine.
- To our knowledge this is the first study in lung cancer radiomics to correlate peritumoral features with response to chemotherapy.
- Combination of intra- and peri-tumoral features appears to better predict response to Chemo for NSCLC.
- Larger, multi-institutional cohort study is needed to validate the applicability of current findings.

Spatial Statistic Aware Segmentation Paradigm: Application on the Prostate Segmentation in the Transrectal Ultrasound Images

Mahdi Orooji^{a,†}, Mehdi Alilou^a, Lee Ponsky^b, Anant Madabhushi^{a,‡}

[†]mxo143@case.edu, [‡]axm788@case.edu

^aCenter for Computational Imaging and Personalized Diagnostics, Case Western Reserve University,

^bUniversity Hospital Case Medical Center, Case Western Reserve University

Abstract—Prostate needle biopsy guided by transrectal ultrasound (TRUS) is the current gold standard for prostate cancer (CaP) detection. An accurate detection of the prostate volume and boundary is influential on diagnosis, treatment, and follow up of CaP. Within this framework, prostate segmentation on TRUS imagery is performed via introduced spatial statistic aware segmentation paradigm. The spatial prior probability is calculated in the training phase, and is used to estimate the texture feature parameters corresponding to the prostate and the background. Estimated parameters is employed to represent an alternative probabilistic presentation of the prostate in TRUS. Results show the 3D prostate capsule is more pronounced in the new representation which ultimately results in more accurate segmentation. Modified active shape model (ASM) is introduced and applied in the new 3D TRUS representation for prostate segmentation.

Index Terms—Prostate Segmentation, Texture Feature Heatmap, Parameter Estimation, Expectation-Maximization, Maximum Likelihood Estimation, Active Shape Model

I. INTRODUCTION

Prostate cancer (CaP) is the second-leading cause of cancer deaths in men and leading cause of cancer deaths men over age 50 in the United States. It is estimated 450,000 new CaP case will be detected by 2015. Predictions also suggest one fourth of new CaP cases will be in men less than 65 years of age which emphasizes the necessity of early detection and localization of CaP. Prostate needle biopsy guided by transrectal ultrasound (TRUS) is the gold standard for CaP diagnosis. Determining the prostate volume and identifying the prostate capsule plays a crucial role in needle targeting. Due to the importance in delineating the prostate on TRUS, semi and fully automated prostate segmentation methods for TRUS imagery have been developed. Despite recent advances in transducer design, resulting in improved spatial and temporal resolution, TRUS image segmentation is still heavily influenced by the quality of data [1], [2]. Additionally, TRUS segmentation is vulnerable to variety of artifacts, such as, different levels of signal attenuation, shadowing artifacts, and speckle. Low contrast between areas of interest is another difficult problem in prostate segmentation on TRUS.

Previous prostate segmentation algorithms for TRUS image have focused on incorporating prior knowledge such as prostate shape [3] or prior spatial probability [4]. Recently, 2D or 3D boundary extraction methods have been developed based

on probabilistic data association filters [2]. However, these approaches assume prior information for the prostate shape (such as concavity) and/or need manually placed initial seed locations inside the prostate [5]. Recently, active contour-based approaches have been used for prostate segmentation. These methods assumed prior spatial properties [6], or needs some initial points on [7] or near [8] the prostate boundary. These methods have also been employed to fuse multi-modal images of the prostate [9]. Our method is a fully automated semi-supervised segmentation algorithm that uses only the spatial prior probability for parameter estimation. Feature parameter estimation considers all voxels in an image; however, segmentation is performed on each voxel independently. Considering joint probability of extracted features and other criteria such as restricted maximum distance of voxels in the segments or morphology of the segments [10], the presented method can be generalized to exploit prior particular available knowledge.

In this work, we formulize a spatial statistic aware segmentation paradigm, and applied it for 3D segmentation of the prostate in the TRUS. Using introduced paradigm, a distribution parameters of 129 texture features in TRUS is estimated and the prostate/background probability heatmap is generated via using estimated distribution. A more informative alternative representation of the prostate in TRUS is introduced, and modified active shape model is applied on it for automatic annotation of the prostate boarder. The rest of the article is organized as follows. After the introduction in the first section, to increase the readability, in the second section the assumptions are described, the parameters are defined, and the problem of matter is formulized. The spatially aware distribution parameter estimation is elevated in the third section. Estimated distribution is employed in the forth section to introduce a new TRUS HeatMap Representation (THR). In section five, a modified adaptive active shape model is introduced and applied on THR. The performance of the method is evaluated in section six and the paper is concluded in section seven.

II. ASSUMPTIONS AND PROBLEM FORMULATION

As a problem statement, the goal is to segment the prostate in a TRUS image slide denoted by I . Note that, I is a 2D axial section of a 3D prostate gland. The 3D capsule

would be reconstructed by stacking the estimated prostate capsule. To increase the readability of the manuscript, we summarize the notation we used in the following. Here and subsequently, \bar{a} , $A_{Y \times X}$, A^\dagger , and $|A|$ imply a is a vector, A is a matrix with Y rows and X columns, a transpose of matrix A , and determinant of matrix A , respectively. Suppose N denotes the total number of voxels of I . By extracting L features from the original intensity image, we can reconstruct an observation matrix, $D_{N \times L} = [\bar{d}_1, \bar{d}_2, \dots, \bar{d}_N]^\dagger$ where the vector $\bar{d}_n = \{d_{n,1}, d_{n,2}, \dots, d_{n,L}\}$ for $n \in \{1, 2, \dots, N\}$ is a feature vector corresponding to each voxel of I . To keep the generality of approach, I is desired to be segmented into K distinct sets of voxels, S_1, \dots, S_K such that the union of all segments cover the entire image, i.e., $\bigcup_{k=1}^K S_k = I$ and $\bigcap_{k=1}^K S_k = \emptyset$. The set of parameters of each segment that needs to be estimated is denoted by $\Theta = \{\mathcal{M}, \Lambda\}$ in which $\mathcal{M}_{K \times L} = [\bar{\mu}_1, \bar{\mu}_2, \dots, \bar{\mu}_K]^\dagger$, for $\bar{\mu}_k = \{\mu_{k,1}, \mu_{k,2}, \dots, \mu_{k,L}\}$ is the mean of the k th segment. $\Lambda^2 = [\Sigma_{1L \times L}^2, \Sigma_{2L \times L}^2, \dots, \Sigma_{KL \times L}^2]$ is the set of covariance matrices of each segments where $\Sigma_k^2 = [\sigma_{k,i,j}^2]$. Table II lists the notations used throughout this paper.

A. Spatial Prior Probability

$\Xi_{N \times K} = [\xi_{n,k}]$, referred to as the *Spatial Prior Probability*, is the likelihood of the n th voxel belonging to k th segment, just based on its spatial information relative to the center of the ultrasound probe in an axial TRUS image. So, $\sum_{k=1}^K \xi_{n,k} = 1$, for any given n . Ξ is calculated from a set of J training studies, where for each study the prostate has been segmented by an expert. The origin for each study is set as the center of the TRUS probe, so that the location of voxels have a consistent position relative to the TRUS probe across all studies. $g_n^{(j)} = i$ for voxel n of j th training image belonging to class k where $k = 1$ represent prostate and $k = 0$ represent background. So, each element of the spatial prior probability matrix is calculated by averaging over all training images as:

$$\xi_{n,k} = \frac{1}{J} \sum_{j=1}^J g_n^{(j,k)} \quad (1)$$

Hence $\xi_{n,1}$ is the frequency of the n th voxel being located in the prostate across J training images.

The prostate is divided into three regions, the apex, the midgland and the base such that they have equal length in the sagittal axis. Two disjoint spatial prior probability was calculated corresponding to the region of interest, one for midgland and another one for the union of the apex and the base.

B. Feature Set Probability

$P_d(\bar{d}_n; \Theta)$ is the probability distribution function (PDF) of a set of features associated with voxel n , given the parameters (which are unknown). Without loss of generality, we assume $P_d(\bar{d}_n; \Theta)$ is modeled as a multivariate Gaussian distribution [4]. Note that even the intensity of the ultrasound image is Rayleigh distributed [11], [12]; however, considering the central limit theorem under weak dependence condition, the

Gaussian distribution of the extracted texture features is a valid assumption [13].

Matrix of Segments: To make the feature set parameters estimation problem tractable, we define an auxiliary (latent) variable $Z_{N \times K} = [z_{n,k}]$, a *Matrix of Segments*, such that any arbitrary n th row of Z has only one element of 1 at k th column which implies n th voxel of I belongs to S_k , and the rest of the elements of the n th row are zero.

Parameter estimation is the solution of the following maximum likelihood equation:

$$\begin{aligned} \hat{\Theta} &= \arg \max_{\Theta} P(D|\Theta, \Xi) \\ &= \arg \max_{\Theta} \sum_Z \log \left(P(D|Z, \Theta, \Xi) P(Z|\Theta, \Xi) \right). \end{aligned} \quad (2)$$

The conditional distribution of the observation matrix given Θ and Z is given by:

$$\begin{aligned} P(D|Z, \Theta, \Xi) &= \prod_{n=1}^N P(\bar{d}_n|Z, \Theta) \\ &= \prod_{n=1}^N \prod_{k=1}^K \left[\frac{1}{(2\pi)^{L/2} |\Sigma_k|} \exp \left((\bar{d}_n - \bar{\mu}_k)^\dagger \Sigma_k^{-2} (\bar{d}_n - \bar{\mu}_k) \right) \right]^{z_{n,k}} \end{aligned} \quad (3)$$

The matrix of segments is independent of the distribution parameters and its probability value is a function of spatial prior probability matrix as follows:

$$P(Z|\Theta, \Xi) = P(Z|\Xi) = \prod_{n=1}^N \prod_{k=1}^K [\xi_{n,k}]^{z_{n,k}} \quad (4)$$

One should note that for other feature distributions rather than Gaussian (such as the distribution of the intensity in TRUS images which is Rayleigh distribution [11], [12]), (3) needs to be substituted by a proper corresponding distribution function.

III. SPATIAL AWARE DISTRIBUTION PARAMETER ESTIMATION

It is assumed that the TRUS image consist of two segments, the prostate and the background. Constrained to the calculated prior spatial probability in (1), we employed an iterative expectation-maximization algorithm to estimate the parameters associated with the prostate and the background in the TRUS for each individual texture feature. In the other words, for a given observation matrix D , we estimate the matrix of parameters, $\{\mathcal{M}, \Lambda^2\}$. Using the estimated parameters, we introduced a new representation of the TRUS in section IV.

It is guaranteed that the expectation-maximization algorithm converges to the local maximum likelihood, however, the convergence of it to the global maximum and the legitimacy of the results is very reliant on the initialization [14].

To improve the parameter estimation, we introduced parameter estimation method, namely Decoupled Maximum Likelihood (DML), that employed the spatial prior probability for a sub-optimum maximum likelihood estimation. The sub-optimum estimated parameters are used an initial estimation of the parameters in the expectation-maximization algorithm. Our assessments shows the introduced method converges to

TABLE I
DESCRIPTION OF NOTATION USED THROUGHOUT THIS PAPER.

Notation	Description	Notation	Description
I	TRUS image scene.	$\Theta = \{\mathcal{M}, \Lambda\}$	Set of actual parameters.
N	Total number of pixels.	$\hat{\Theta} = \{\hat{\mathcal{M}}, \hat{\Lambda}\}$	Set of estimated parameters.
L	Total number of extracted features.	$\bar{\mu}_k = [\mu_{k,l}]_{1 \times L}$	Vector of actual means of k th segment.
K	Assumed number of segments.	$\hat{\mu}_k = [\hat{\mu}_{k,l}]_{1 \times L}$	Vector of estimated means of k th segment.
$D_{N \times L}$	Matrix of observations.	$\Sigma_k^2 = [\sigma_{k,i,j}^2]_{L \times L}$	Set of actual covariance matrix of k th segment.
\bar{d}_n	Features vector of n th voxel.	$\hat{\Sigma}_k^2 = [\hat{\sigma}_{k,i,j}^2]_{L \times L}$	Set of estimated covariance matrix of k th segment.
$\Xi = [\xi_{n,k}]_{N \times K}$	Spatial prior probability matrix.	$I_f(\theta)$	Fisher Information of parameter θ .

the global maximum with less number of the iterations and does not trap on the local maximum.

A. Decoupled Maximum Likelihood (DML) Approach for Initial Estimation of the Parameters

By substituting corresponding values from (3) and (4) into (2), one can note that the maximum likelihood problem does not have an analytical closed form solution. When the analytical solution does not exist, generalized maximum likelihood ratio test (GLRT) is proposed [15]. GLRT is not an optimum solution, because instead of maximizing the likelihood ratio, independently treats the nominator and the denominators of the likelihood ratio and maximize them separately [16]. So, it results in the sub-optimum answer. Using GLRT algorithm, we introduced the decoupled maximum likelihood to estimate the parameters of the nominator (corresponding to the prostate) and the denominator (corresponding to the background) separately. The algorithm is as follows.

The parameters of k th segment is denoted by $\theta_k \triangleq \{\bar{\mu}_k, \Sigma_k^2\}$ for $k = 1$ and 2 corresponding to the background and the prostate, respectively. $\hat{\theta}_k^{(DML)}$ are estimated parameters of k th segment obtained by and decoupled maximum likelihood approach. So,

$$\hat{\theta}_k^{(DML)} = \arg \max_{\theta_k} P(D|\theta_k, \Xi), \text{ for } 1 \leq k \leq K \quad (5)$$

From (5), it is implied that the parameter estimation problem for each segment is decoupled to become tractable. To solve (5) we have,

$$P(D|\theta_k, \Xi) = \prod_{n=1}^N \left[\frac{1}{(2\pi)^L |\Sigma_k|} \exp \left(-(\bar{d}_n - \bar{\mu}_k)^\dagger \Sigma_k^{-2} (\bar{d}_n - \bar{\mu}_k) \right) \right]^{\xi_{n,k}} \quad (6)$$

After some manipulation one can show that the solution of DML parameter estimation from (6) is given by:

$$\frac{\partial}{\partial \bar{\mu}_k} P(D|\theta_k, \Xi) = 0 \implies \hat{\bar{\mu}}_k = \frac{\sum_{n=1}^N \xi_{n,k} \bar{d}_n}{\sum_{n=1}^N \xi_{n,k}} \quad (7)$$

$$\frac{\partial}{\partial \Sigma_k^2} P(D|\theta_k, \Xi) = 0 \implies \hat{\Sigma}_k^2 = \frac{\sum_{n=1}^N \xi_{n,k} (\bar{d}_n - \hat{\bar{\mu}}_k)^2}{\sum_{n=1}^N \xi_{n,k}} \quad (8)$$

The estimated mean and variance from (7) and (8) are employed as an initial mean and variance in the next step.

B. Parameters Estimation Per Individual Texture Feature

The solution of the Maximum Likelihood (ML) Ratio Test for each texture feature is the optimum unsupervised parameter estimation approach [15], [17]. However, ML is too complicated to be derived analytically. Hence, we employ an iterative algorithm, inspired by the Expectation-Maximization (EM) mixture model parameter estimation approach, to estimate values of Θ . EM is a powerful iterative algorithm to estimate the parameters of the mixture models when the associated log-likelihood maximization problem is too complicated to solve analytically. Using the same approach, we modified the two steps of Expectation and Maximization as follows:

Expectation Step: Current and revised estimation of Θ are denoted by Θ^{OLD} and Θ^{NEW} , respectively. The conditional expectation of $\log P(D, Z|\Theta)$ given D and the current estimation of Θ is given by,

$$\begin{aligned} \mathcal{Q}(\Theta; \Theta^{\text{OLD}}) &= E_Z [\log P(D, Z|\Theta)] \\ &= \sum_{n=1}^N \sum_{k=1}^K E_Z [z_{n,k} | D, \Theta^{\text{OLD}}] \times \\ &\quad \left(\log \xi_{n,k} - \frac{L}{2} \log 2\pi - \log |\Sigma| + (\bar{d}_n - \bar{\mu}_k)^\dagger \Sigma_k^{-2} (\bar{d}_n - \bar{\mu}_k) \right) \end{aligned} \quad (9)$$

where $E_z[\cdot|x]$ is the conditional expectation given x , respect to z . After some manipulation one can show that:

$$\begin{aligned} \gamma_{n,k} &\triangleq E_Z [z_{n,k} | D, \Theta^{\text{OLD}}] \\ &= \frac{\xi_{n,k} P(\bar{d}_n | z_{n,k}, \Theta^{\text{OLD}})}{\sum_{k=1}^K \xi_{n,k} P(\bar{d}_n | z_{n,k}, \Theta^{\text{OLD}})} \end{aligned} \quad (10)$$

Maximization Step: It has been shown in [18] that the log-likelihood function is the monotone increasing function of the number of EM iteration steps. So, regardless of the initial value of Θ , EM converges. Θ^{NEW} , the new values of parameters, are the solution of:

$$\Theta^{\text{NEW}} = \arg \max_{\Theta} \mathcal{Q}(\Theta, \Theta^{\text{OLD}}) \quad (11)$$

By calculating the partial derivative of (9) and (10) respect to $\bar{\mu}_k$ and Σ_k , one can show that

$$\hat{\mu}_{k,l} = \frac{\sum_{n=1}^N \gamma_{n,k} d_{n,l}}{\sum_{n=1}^N \gamma_{n,k}}, \quad (12)$$

$$\hat{\sigma}_{k,l}^2 = \frac{\sum_{n=1}^N \gamma_{n,k} (d_{n,l} - \mu_{k,l})^2}{\sum_{n=1}^N \gamma_{n,k}} \quad (13)$$

IV. TRSU HEATMAP REPRESENTATION (THR)

Prostate segmentation in TRUS is a challenging task mainly due to the high inherent noise of the ultrasound images [19]. On the other side, the proficiency of the texture features in the prostate segmentation is already investigated [20]. We employed the power of the texture features in presenting the prostate in the ultrasound images and also the spatial statistics information to introduce an alternative representation of the TRUS image, in which the prostate capsule is more pronounced in compare to the original TRUS image. We named it the *TRUS-HeatMap Representation (THR)*.

To generate the THM representation, we need to generate the heatmap probability of the foreground and the background per feature. To do so, the first step is calculating the spatial prior probability by substituting the prostate capsule annotations in (1). Because the size of the prostate capsule in the apex and the base are close and it is relatively smaller than the size of the prostate in the midgland [21], so, we generated two disjoint spatial prior probability model for two sets of the apex/based and midgland.

In the second step texture features were extracted for a given TRUS image. In this article we employed total of 129 texture features which described in Table II. Considering the spatial prior probability, in the third step we employed the Spatially Aware Distribution Parameter Estimation Method introduced in section III to answer which segments in conjunction with which set of parameters are going to maximize the likelihood of observed extracted texture features of a TRUS image. To improve the proficiency of EM-based parameter estimation method, as it was described in the subsection III-A, we included the Decoupled Maximum Likelihood approach for initial estimation of the parameters in the third step.

And finally in the fourth step, the estimated distribution parameters corresponding to the foreground and the background for each feature is used to generate the foreground and the background probability heatmap. Figure 1 demonstrates the heatmap generation schematic for a texture feature. Figure 2 demonstrates the heatmap of the prostate and the background for Haralick features [22].

A. Adaptive Combination of the Texture Feature's Heatmaps to Generate THR

After calculating the probability heatmap of the foreground and the background for each feature, we need to find which feature in the foreground and which feature in the background has the highest capability of the prostate segmentation. To do so, we need to define a proficiency metric for foreground heatmaps and the background heatmaps.

$$\phi_{Pr} \triangleq \frac{\sum_{\forall n} z_{n,1} f^{Pr}(d_n)}{\sum_{\forall n} z_{n,1}} \quad (14)$$

$$\phi_{Bk} \triangleq \frac{\sum_{\forall n} z_{n,0} (1 - f^{Pr}(d_n))}{\sum_{\forall n} z_{n,0}} \quad (15)$$

By combining the estimated probability of the prostate and the estimated probability of the background, we generated the prostate probability heatmap. Defined proficiency metric is employed to find the most proficient texture features for discriminating the prostate from the background. So, we added the proficiency weighted heatmaps to obtain the final prostate heatmap. Finally, AAM is applied on the prostate probability heatmap from the previous step for prostate segmentation in TRUS. Figure 3 demonstrates the prostate heatmap.

B. Calculating the Heat-map

Estimated features parameters, $\hat{\Theta}$, induce maximum likelihood image segmentation regardless of the parameter estimation approach (DML or ML). The prostate heat-map is defined as the conditional probability (given estimated parameters) that a voxel n belongs to the prostate which would be:

$$P(z_{n,1} = 1 | \hat{\Theta}) \quad (16)$$

$$= \frac{1}{\mathfrak{F}} \left[\xi_{n,1} P(\bar{d}_n | \hat{\mu}_1, \hat{\Sigma}_1^2) + \xi_{n,0} \left(1 - P(\bar{d}_n | \hat{\mu}_0, \hat{\Sigma}_0^2) \right) \right]$$

where \mathfrak{F} is a normalization factor to guarantee that the heatmap values are in the range of 0 to 1.

V. ADAPTIVE ACTIVE SHAPE MODEL ON TRSU HEATMAP

VI. EXPERIMENTAL RESULTS

A. Dataset

The presented EM-based segmentation method was applied on 3D Transrectal Ultrasound (TRUS) images for six patients. TRUS images was acquired using a bi-planer side-firing transrectal probe. A prostate boundary on TRUS was manually delineated by an expert radiologist. To correct for the possible TRUS attenuation artifacts (due to the fact that pixels closer to the probe appear brighter), we employed the method in [4].

REFERENCES

- [1] S. Ghose, J. Mitra, A. Oliver, R. Mart, X. Llad, J. Freixenet, J. Vilanova, J. Comet, D. Sidib, and F. Meriaudeau, "Advanced concepts for intelligent vision systems," ser. Lecture Notes in Computer Science, J. Blanc-Talon, W. Philips, D. Popescu, P. Scheunders, and P. Zemk, Eds. Springer Berlin Heidelberg, 2012, vol. 7517, pp. 190–200. [Online]. Available: http://dx.doi.org/10.1007/978-3-642-33140-4_17
- [2] R. M. X. L. J. C. V. J. F. J. M. D. S. F. M. Soumya Ghose, Arnau Oliver, "A survey of prostate segmentation methodologies in ultrasound, magnetic resonance and computed tomography images," *Computer Methods and Programs in Biomedicine*, vol. 108, no. 1, pp. 262–287, 2012.
- [3] W. Qiu, J. Yuan, E. Ukwatta, D. Tessier, and A. Fenster, "Three-dimensional prostate segmentation using level set with shape constraint based on rotational slices for 3d end-firing trus guided biopsy," *Medical Image Computing and Computer-Assisted Intervention MICCAI 2012*, vol. 1, 2012.
- [4] R. Sparks and et al., "Fully automated prostate magnetic resonance imaging and transrectal ultrasound fusion via a probabilistic registration metric," in *Proceedings of the SPIE*, vol. 8671, 2013.

TABLE II
DESCRIPTION OF THE TEXTURE FEATURES USED FOR PROSTATE SEGMENTATION IN TRUS.

Feature category	Descriptor	Intuitive Description
Haralick features (Repeated occurrence of grey level configuration in the texture represented via the grey-level co-occurrence matrix (GLCM), which varies rapidly with distance in fine textures and slowly in large textures)	Inverse Difference Moment (IDM)	IDM is a reflection of the presence or absence of uniformity, and hence is a measure of local regions of homogeneity High IDM: Higher presence of locally uniform windows in GLCM Low IDM: Higher presence of locally heterogeneous windows in GLCM
	Correlation	Quantifies the linear patterns in an image based on the distance parameter.
	Sum Entropy	Measure of GLCM relationship to distribution of intensity with respect to entropy. Entropy is the measure of disorder.
	Sum Variance	Measure of GLCM relationship to distribution of intensity with respect to variance High sum variance: greater standard deviation of sum average Low sum variance: low standard deviation of sum average
Laws features	E5, L5, S5	Combining E- Edges, L- Level and S- Spots in both X any Y directions
Laplacian pyramids		Multi-resolution filters capture edges at different levels
Gray level features		The basic, intensity based features including mean, median, range and standard deviation.
Gabor Features		Oriented textures via changes in direction and scale; capture microarchitectures
Gradient Features		Represent the directional change in the intensity values of pixels in the ROI
Local Binary Pattern		Thresholding the window with the center pixel value.

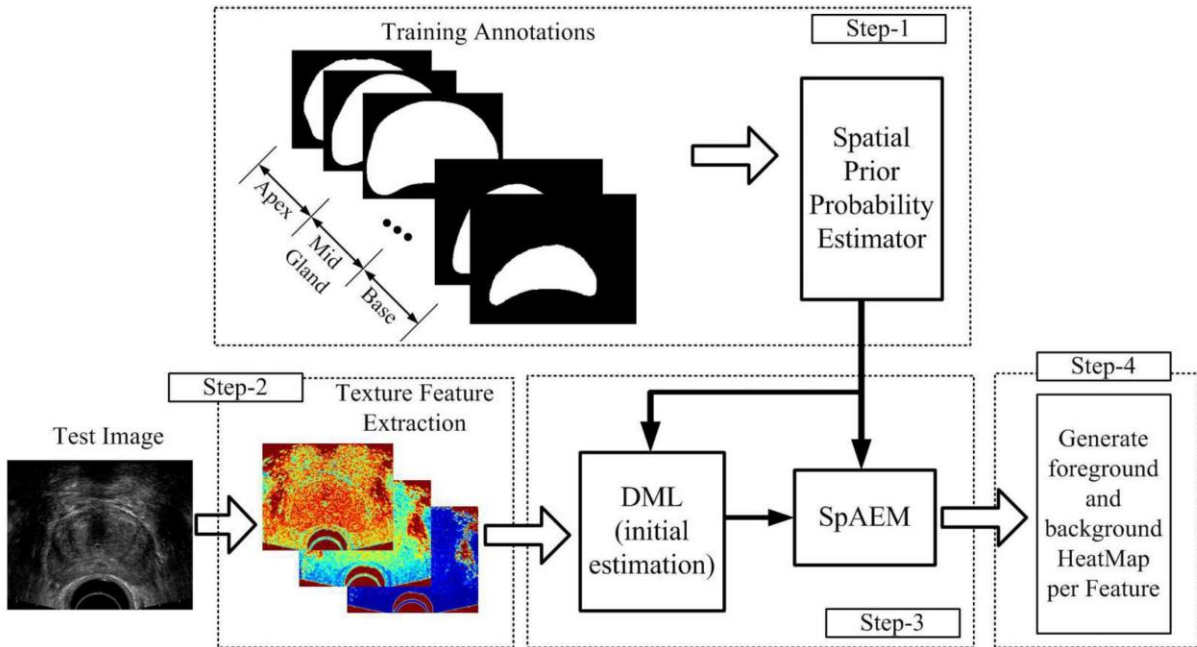


Fig. 1. Schematic of four steps used for generating the foreground and background heat-map per texture feature.

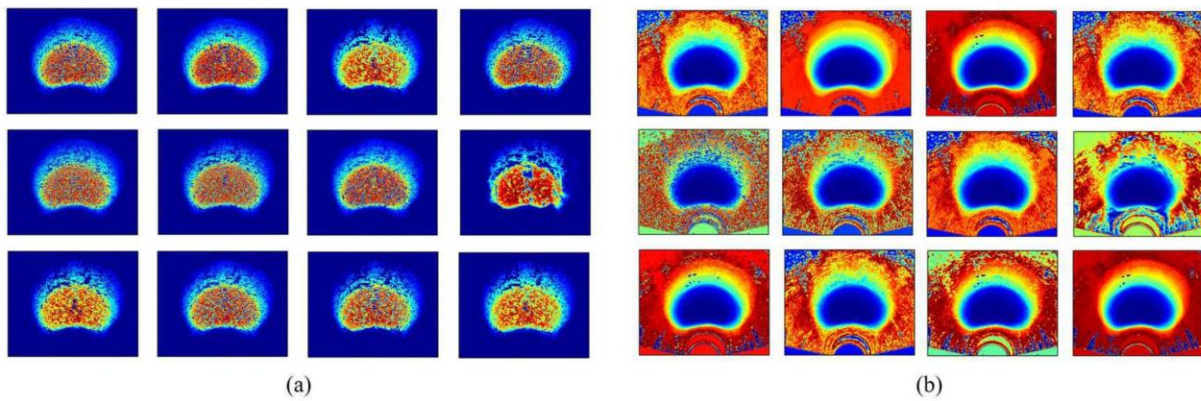


Fig. 2. The probability heatmap of (a) the foreground probability and (b) the background probability.

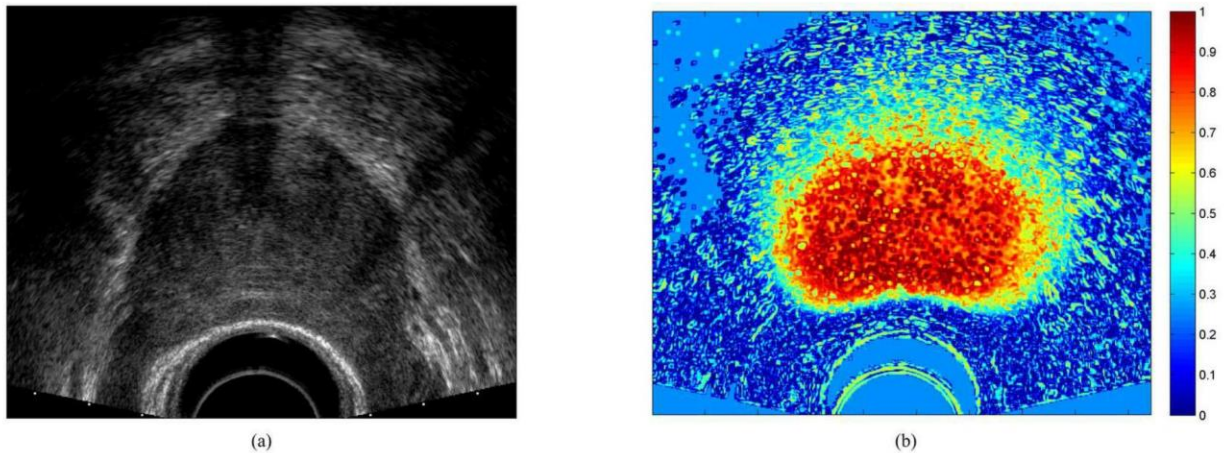


Fig. 3. (a) TRUS images of a prostate and (b) corresponding the prostate heatmap.

- [5] P. Abolmaesumi and et al., "An interacting multiple model probabilistic data association filter for cavity boundary extraction from ultrasound images," *Medical Imaging, IEEE Transactions on*, vol. 23, no. 6, pp. 772–784, 2004.
- [6] J. Xu, J. P. Monaco, and A. Madabhushi, "Markov random field driven region-based active contour model (marace): application to medical image segmentation," in *Proceedings of the 13th international conference on Medical image computing and computer-assisted intervention: Part III*, ser. MICCAI'10. Berlin, Heidelberg: Springer-Verlag, 2010, pp. 197–204. [Online]. Available: <http://dl.acm.org/citation.cfm?id=1926877.1926903>
- [7] J. Yezzi, A., S. Kichenassamy, A. Kumar, P. Olver, and A. Tannenbaum, "A geometric snake model for segmentation of medical imagery," *Medical Imaging, IEEE Transactions on*, vol. 16, no. 2, pp. 199–209, 1997.
- [8] Y. Yu, J. A. Molloy, and S. Acton, "Segmentation of the prostate from suprapubic ultrasound images," *Medical Physics*, vol. 1, 2004.
- [9] S. S. Mahdavi, , and et al., "Fusion of ultrasound b-mode and vibro-elastography images for automatic 3-d segmentation of the prostate," *Medical Imaging, IEEE Transactions on*, vol. 31, no. 11, pp. 2073–2082, 2012.
- [10] C. Carson and et al., "Blobworld: image segmentation using expectation-maximization and its application to image querying," *Pattern Analysis and Machine Intelligence, IEEE Transactions on*, vol. 24, no. 8, pp. 1026–1038, 2002.
- [11] J. Goodman, *Speckle Phenomena in Optics: Theory and Applications*. Roberts & Company, 2007. [Online]. Available: <http://books.google.com/books?id=TynXEcS0DncC>
- [12] A. Sarti, C. Corsi, E. Mazzini, and C. Lamberti, "Maximum likelihood segmentation of ultrasound images with rayleigh distribution," *Ultrasonics, Ferroelectrics, and Frequency Control, IEEE Transactions on*, vol. 52, no. 6, pp. 947–960, June 2005.
- [13] B. Rosen, "On the central limit theorem for sums of dependent random variables," *Zeitschrift fr Wahrscheinlichkeitstheorie und Verwandte Gebiete*, vol. 7, no. 1, pp. 48–82, 1967.
- [14] C. F. J. Wu, "On the convergence properties of the em algorithm," *The Annals of Statistics*, vol. 11, no. 1, pp. pp. 95–103, 1983.
- [15] H. L. V. Trees, *Detection, Estimation, and Modulation Theory: Radar-Sonar Signal Processing and Gaussian Signals in Noise*. Melbourne, FL, USA: Krieger Publishing Co., Inc., 1992.
- [16] O. Zeitouni, J. Ziv, and N. Merhav, "When is the generalized likelihood ratio test optimal?" *Information Theory, IEEE Transactions on*, vol. 38, no. 5, pp. 1597–1602, 1992.
- [17] J. Neyman and E. S. Pearson, "On the use and interpretation of certain test criteria for purposes of statistical inference: Part i," *Biometrika*, vol. 20A, no. 1/2, pp. pp. 175–240, 1928. [Online]. Available: <http://www.jstor.org/stable/2331945>
- [18] C. M. Bishop, *Pattern Recognition and Machine Learning (Information Science and Statistics)*. Secaucus, NJ, USA: Springer-Verlag New York, Inc., 2013.
- [19] O. Michailovich and A. Tannenbaum, "Despeckling of medical ultrasound images," *Ultrasonics, Ferroelectrics, and Frequency Control, IEEE Transactions on*, vol. 53, no. 1, pp. 64–78, Jan 2006.
- [20] Y. Zhan and D. Shen, "Deformable segmentation of 3-d ultrasound prostate images using statistical texture matching method," *Medical*

Part 3: Proof of Registration



Mahdi Orooji <mxo143@case.edu>

Registration Confirmation and Receipt #937388

1 message

ASCO Annual Meeting Registration <ascoregistration@spargoinc.com>
To: mxo143@case.edu

Thu, Jun 2, 2016 at 7:17 PM

ASCO ANNUAL MEETING
**COLLECTIVE
WISDOM**

REGISTRATION CONFIRMATION

June 3-7, 2016

Pre-Annual Meeting Educational Programs: June 2-3

Exhibits: June 4-6

McCormick Place | Chicago, Illinois

Please use this bar code, in print or on your phone, onsite in order to print your badge!



[View it on your Phone](#)

Registration Confirmation and Receipt #937388

ASCO Annual Meeting
June 03 - June 7, 2016
McCormick place
Chicago, IL

Registration Confirmation Number/Badge ID: 937388

Date of Registration: 06/02/2016

Registration Type: Attendee

Name: Mahdi Orooji, PhD

Company: Case Western Reserve University

Address: 523 Wickenden Building, 10900 Euclid Ave

Address 2: case western reserve university

City/State/Zip: Cleveland, OH 44106

Country: USA

Phone: 2256109702

Mobile Phone: [\(225\) 610-9702](tel:2256109702)

Email: mxo143@case.edu

[Cancellations/Changes](#)

Select here for registration changes and information

[Hotel Information](#)

Select here for hotel reservations and information

[Travel Information](#)

Select here for travel and ground transportation information

Keep Up With the Latest



Thank you for registering for the 2016 ASCO Annual Meeting to be held at McCormick Place in Chicago, Illinois. Please take a moment to review the information in this confirmation to confirm that it is correct. This is both your confirmation and your receipt. Please print and retain this document for your records.

REGISTRATION
Annual Meeting Registration with Virtual Meeting
\$170.00



US 20160155225A1

(19) **United States**
 (12) **Patent Application Publication** (10) **Pub. No.: US 2016/0155225 A1**
Madabhushi et al. (43) **Pub. Date: Jun. 2, 2016**

(54) **TEXTURAL ANALYSIS OF LUNG NODULES** *A61B 6/00* (2006.01)
G06T 7/40 (2006.01)
 (71) Applicant: **Case Western Reserve University**, Cleveland, OH (US) (52) **U.S. CL.**
 CPC *G06T 7/0012* (2013.01); *G06T 7/0081* (2013.01); *G06T 7/40* (2013.01); *A61B 6/032* (2013.01); *A61B 6/50* (2013.01); *G06T 2207/10081* (2013.01); *G06T 2207/30064* (2013.01); *G06T 2207/30096* (2013.01)
 (72) Inventors: **Anant Madabhushi**, Shaker Heights, OH (US); **Mirabela Rusu**, Cleveland, OH (US); **Mahdi Orooji**, Cleveland, OH (US); **Mehdi Allou**, Cleveland, OH (US)

(21) Appl. No.: **14/873,611**

(22) Filed: **Oct. 2, 2015**

Related U.S. Application Data

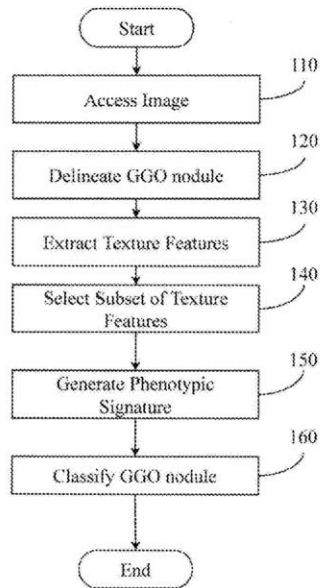
(60) Provisional application No. 62/085,616, filed on Nov. 30, 2014.

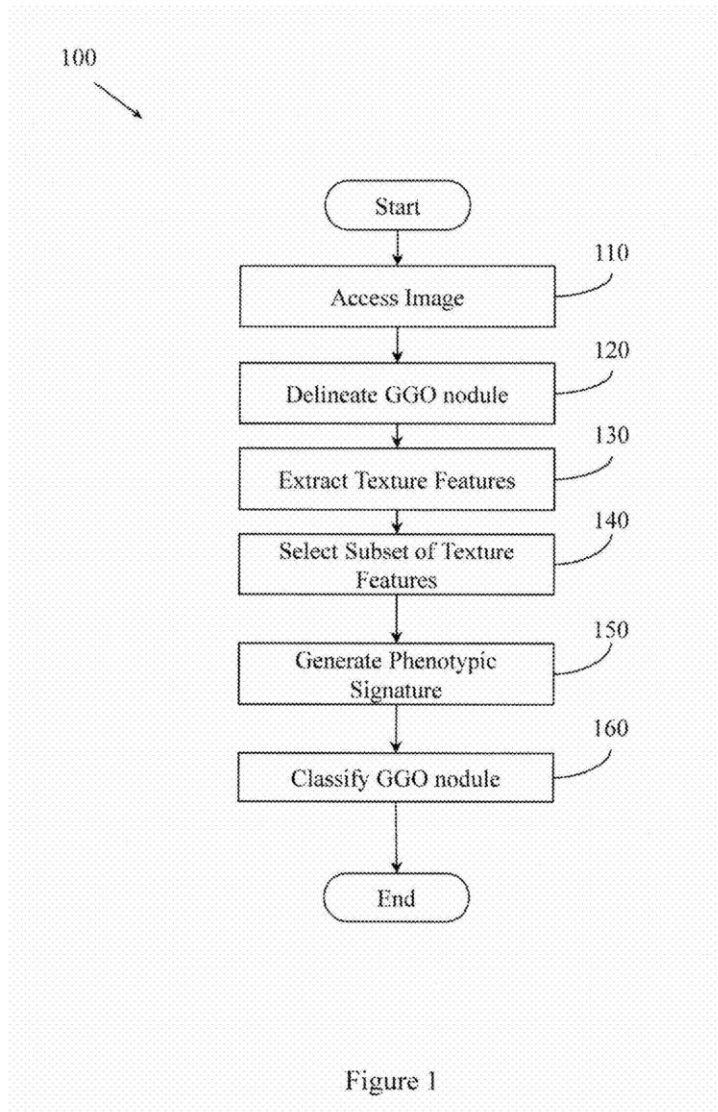
Publication Classification

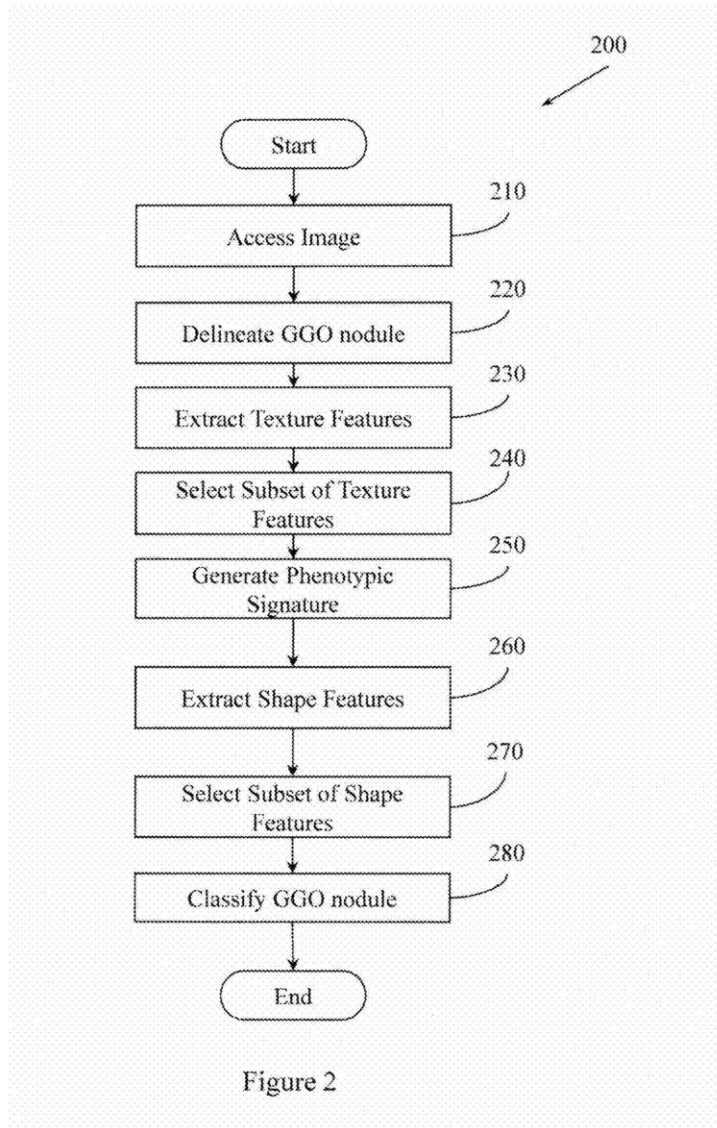
(51) **Int. CL.**
G06T 7/00 (2006.01)
A61B 6/03 (2006.01)

(57) **ABSTRACT**
 Methods, apparatus, and other embodiments associated with classifying a region of tissue using textural analysis are described. One example apparatus includes an image acquisition logic that acquires an image of a region of tissue demonstrating GGO nodule pathology, a delineation logic that distinguishes GGO nodule tissue within the image from the background of the image, a texture logic that extracts a set of texture features from the image, a phenotypic signature logic that computes a phenotypic signature from the image, a shape logic that extracts a set of shape features from the image, and a classification logic that classifies the GGO nodule tissue based, at least in part, on the set of texture features, the phenotypic signature, or the set of shape features. A prognosis for a patient may be provided based on the classification of the image.

100







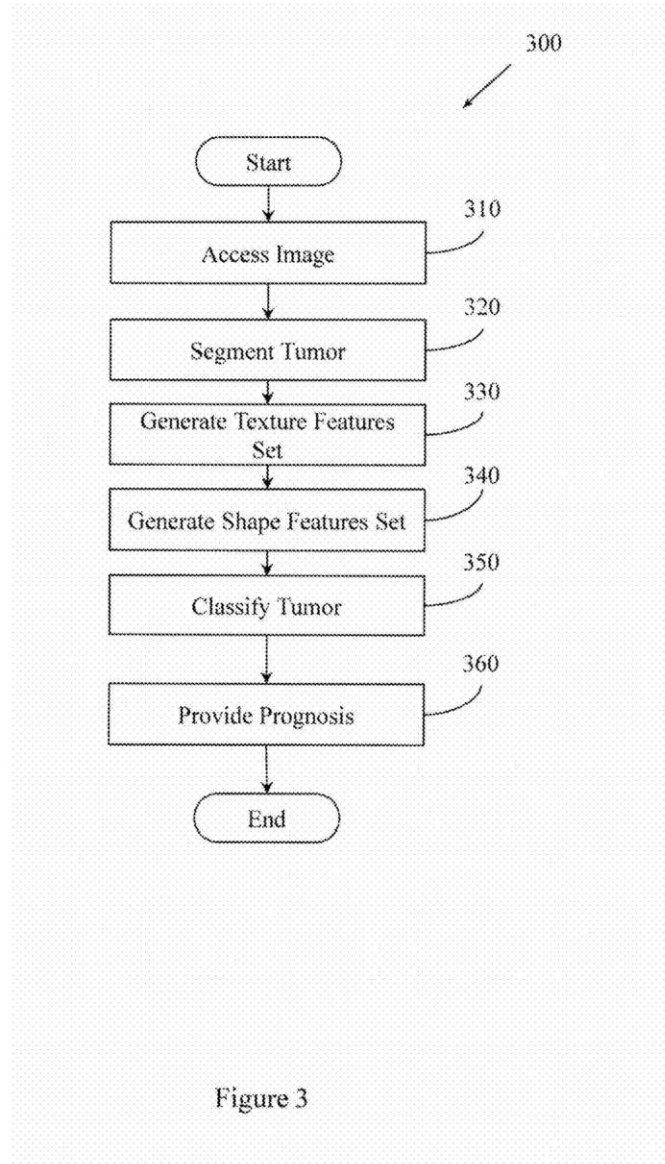


Figure 3

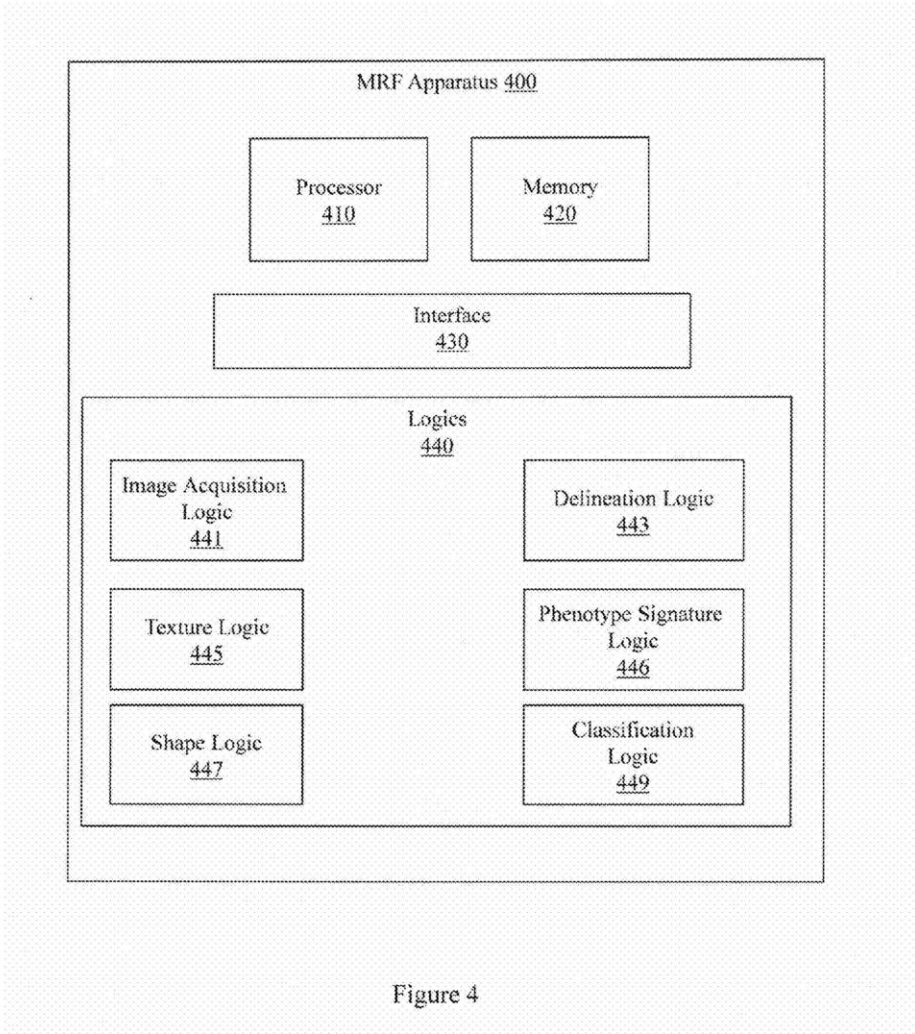


Figure 4

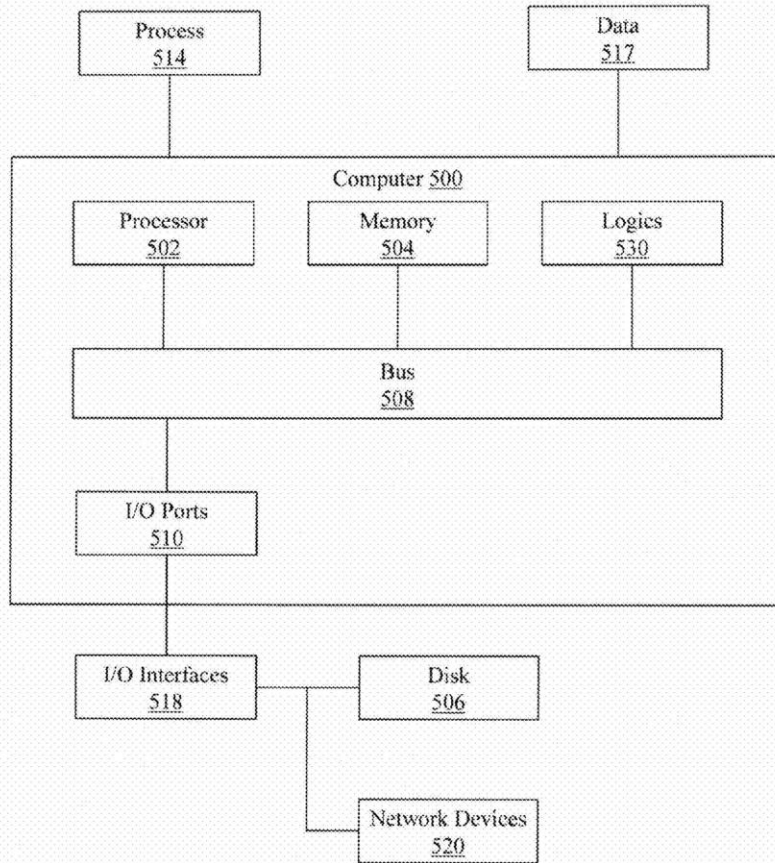


Figure 5

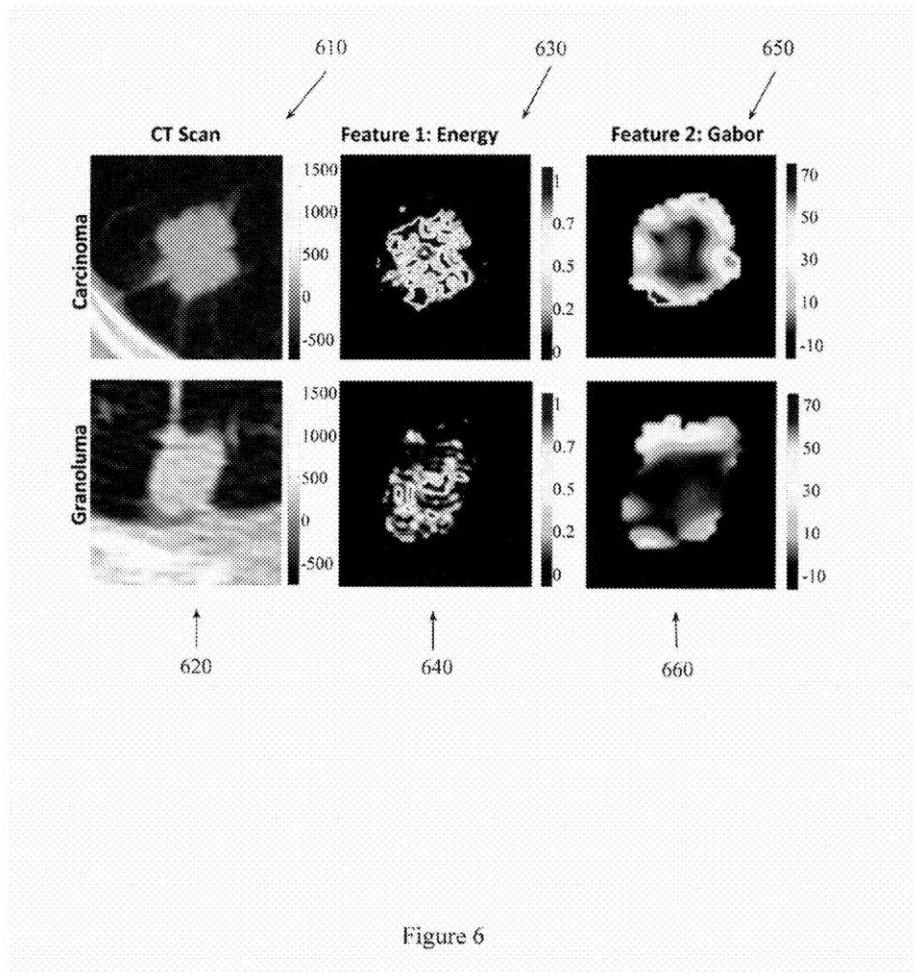
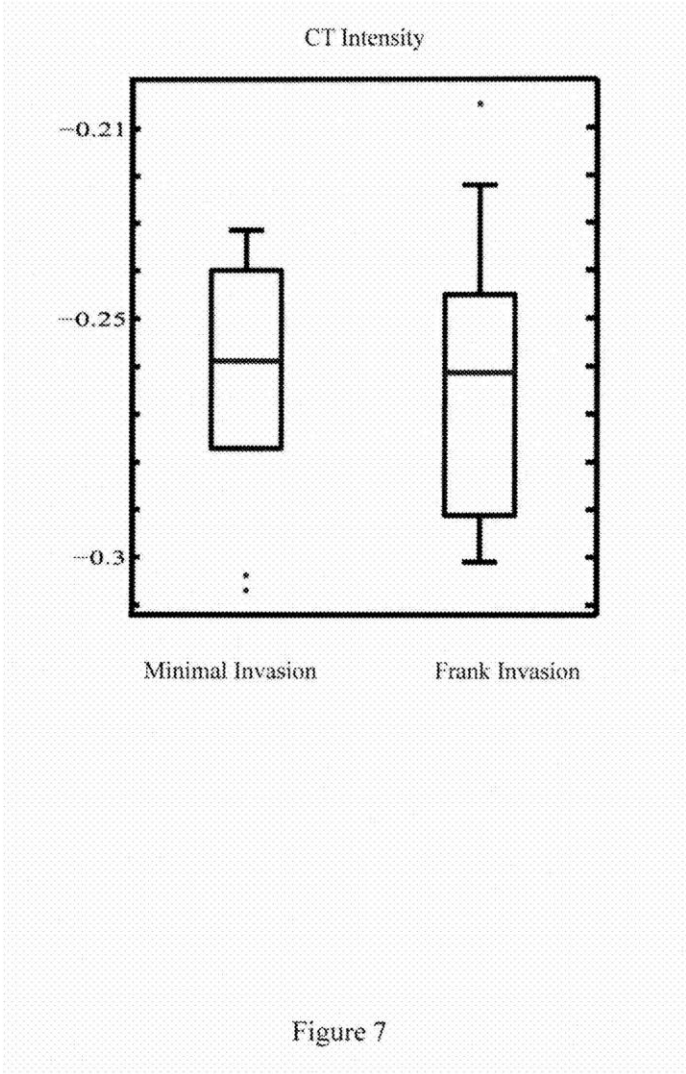
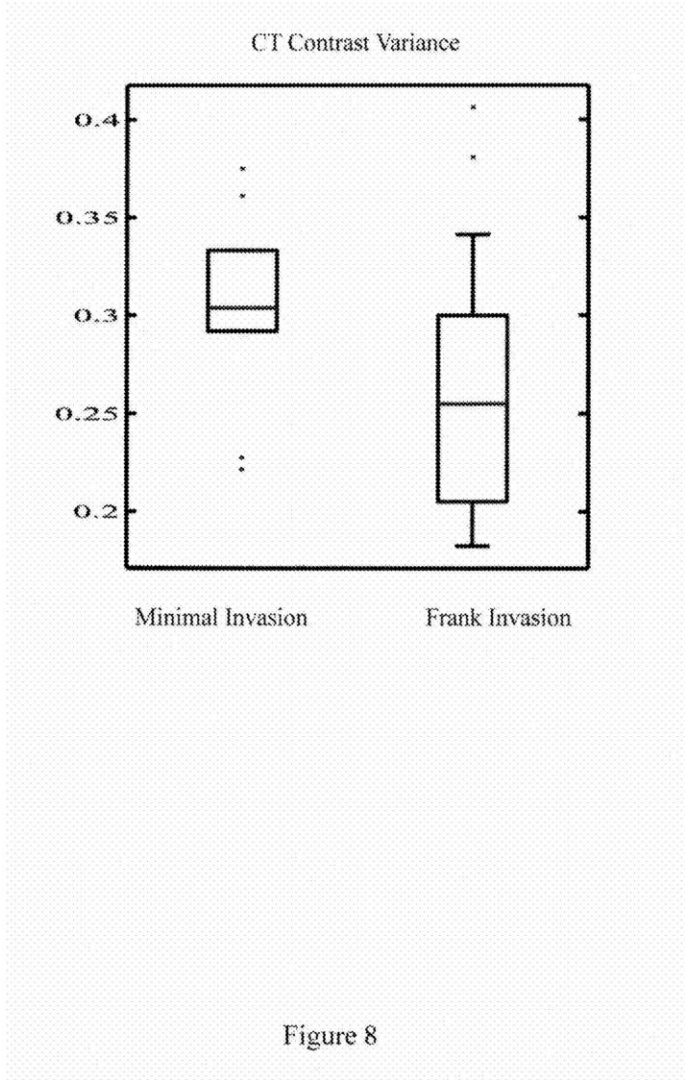


Figure 6





TEXTURAL ANALYSIS OF LUNG NODULES

CROSS REFERENCE TO RELATED APPLICATIONS

[0001] This application claims the benefit of U.S. Provisional Application 62/085,616 filed Nov. 30, 2014.

BACKGROUND

[0002] Variations of lung nodule invasiveness and morphology relate to prognosis and patient outcomes. One approach for diagnosing cancer is histopathological examination of biopsy tissue. The examination may produce a diagnostic profile based on attributes including cell morphology, cytoplasmic changes, cell density, and cell distribution. Visual characterization of tumor morphology is, however, time consuming and expensive. Visual characterization is also subjective and thus suffers from inter-rater and intra-rater variability. Conventional visual characterization of lung nodule morphology by a human pathologist may therefore be less than optimal in clinical situations where timely and accurate classification can affect patient outcomes.

[0003] Computerized tomography (CT) is used to image nodules in lungs. Chest CT imagery may be used to detect and diagnose non-small cell lung cancer. However, conventional approaches have been challenged when defining radiographic characteristics that reliably describe the degree of invasion of early non-small cell lung cancers with ground glass opacity (GGO). For example, conventional CT imagery based approaches may find it difficult, if even possible at all, to reliably discriminate nodules caused by benign fungal infections from non-small cell lung cancer nodules.

[0004] The degree of invasion of a lung nodule is correlated with prognosis. For example, patients suffering from minimally invasive nodules may have higher disease free survival rate at five years compared to patients with nodules demonstrating frank invasion. Since radiologists may be challenged to reliably distinguish the level of invasiveness of lung nodules in situ using conventional CT approaches in clinically optimal or relevant time frames, invasive procedures that may be performed that ultimately result in a negative diagnosis. These invasive procedures take time, cost money, and put a patient at additional risk.

BRIEF DESCRIPTION OF THE DRAWINGS

[0005] The accompanying drawings, which are incorporated in and constitute a part of the specification, illustrate various example apparatus, methods, and other example embodiments of various aspects of the invention. It will be appreciated that the illustrated element boundaries (e.g., boxes, groups of boxes, or other shapes) in the figures represent one example of the boundaries. One of ordinary skill in the art will appreciate that in some examples one element may be designed as multiple elements or that multiple elements may be designed as one element. In some examples, an element shown as an internal component of another element may be implemented as an external component and vice versa. Furthermore, elements may not be drawn to scale.

[0006] FIG. 1 illustrates an example method of characterizing a GGO nodule in a region of lung tissue.

[0007] FIG. 2 illustrates an example method of characterizing a GGO nodule in a region of lung tissue.

[0008] FIG. 3 illustrates an example method of distinguishing invasive tumors from non-invasive tumors in chest CT images.

[0009] FIG. 4 illustrates an example apparatus that classifies a region of tissue in an image.

[0010] FIG. 5 illustrates an example computer in which example methods and apparatus described herein operate.

[0011] FIG. 6 illustrates textural features of a CT image of a granuloma and a carcinoma.

[0012] FIG. 7 is a boxplot of CT intensities of a CT image of a minimally invasive GGO nodule and a frank invasive GGO nodule.

[0013] FIG. 8 is a boxplot of CT contrast variance of a CT image of minimally invasive GGO nodule and frank invasive GGO nodule.

DETAILED DESCRIPTION

[0014] Variations in tumor invasiveness and morphology may be related to patient prognosis and outcome. In particular, a GGO nodule's level of invasion is strongly correlated to patient prognosis. Conventional methods of diagnosing cancer include visual histopathological examination of a biopsy to create a diagnostic profile based on variations in tumor morphology. However, invasive biopsy may not always be a convenient or appropriate method for assessing GGO nodules. Invasive biopsies cost money, take time, and put a patient at additional risk. A non-invasive approach that provided improved accuracy compared to conventional CT based approaches would reduce the number of unnecessary interventions, reduce the dependency on repetitive or higher resolution CT exams, offer a non-invasive means of assessing response to targeted therapies, and improve patient outcomes. Thus, a timely, non-invasive procedure that results in more accurate discrimination between minimally invasive and frank invasive nodules would offer reduced risk to patients while providing economic benefits to the health care system.

[0015] CT imagery is conventionally used to differentiate malignant GGO nodules from other, non-cancerous GGO nodules. Conventional methods of visually assessing GGO nodule invasiveness based on CT imagery are subjective and yield intra and inter-reviewer variability. In one example, of a group of baseline CT chest scans, 51% were found positive for lung nodules. However, only 12% of those lung nodules were found to be malignant. The remainder were determined to be granulomas due to a prior histoplasmosis infection. Conventional CT approaches may focus exclusively on detection of lung nodules, or exclusively on diagnosing malignancy via CT scans. Example apparatus and methods discriminate granulomas caused by fungal infection from carcinomas. Distinguishing fungal infection from carcinoma facilitates reducing surgical interventions that ultimately result in a diagnosis of histoplasmosis.

[0016] Example methods and apparatus more accurately distinguish malignant GGO nodules from benign nodules. Since a more accurate distinction is made, example apparatus and methods thus predict patient outcomes in a more consistent and reproducible manner. Example methods and apparatus predict patient outcomes more accurately than conventional methods by employing computerized textural and morphologic analysis of lung CT imagery to distinguish granulomas due to fungal infection from malignant tumors. A GGO nodule may be segmented from an image background. Features may be automatically extracted from the segmented GGO nodule image. Example methods and apparatus may

extract texture features and shape features from the GGO nodule image. Example methods and apparatus may also extract tortuosity features from the GGO nodule image. Malignant lung tumors may induce irregular changes to vessel shapes. Example methods and apparatus detect and quantify vessel tortuosity abnormalities on a tumor neighborhood. A subset of extracted features may be selected using principal component analysis (PCA) and then a classification of the GGO nodule image may be generated using linear discriminant analysis (LDA) or quadratic discriminant analysis (QDA).

[0017] Carcinomas may have a more chaotic cellular architecture than granuloma. The chaotic cellular architecture may be correlated to an energy feature in an image. The energy feature may be represented as a texture feature or a shape feature. In some embodiments, the energy feature is more pronounced in a CT heatmap of a cancerous GGO nodule than in a CT heatmap of a granuloma because of the more chaotic cellular architecture of the cancerous GGO nodule. FIG. 6 illustrates this property of cancerous GGO nodules compared with granuloma GGO nodules that were caused by benign fungal infections. The chaotic cellular architecture may also be correlated to tortuosity features of vessels associated with a tumor or a GGO nodule.

[0018] FIG. 6 illustrates, at 610, a CT scan image of a cancerous GGO nodule identified as a carcinoma. FIG. 6 also illustrates, at 620, a CT scan image of GGO nodule identified as a granuloma. FIG. 6 illustrates, at 630, an energy textural feature extracted from intensity values of image 610 of the cancerous GGO nodule. The energy of a textural feature measures local homogeneity within the image, illustrating how uniform the texture is. FIG. 6 also illustrates a textural feature image 640 of the energy extracted from the image of the benign granuloma 620. The energy feature image 630 of the cancerous GGO nodule displays a more pronounced energy feature than the benign granuloma texture feature image 640, which demonstrates the more chaotic cellular architecture of a cancerous GGO nodule. FIG. 6 also illustrates, at 650, a heatmap of a Gabor feature of the cancerous GGO nodule. The Gabor feature represents texture using a sinusoidal plane wave modulated Gaussian kernel function. FIG. 6 further illustrates, at 660, a heatmap of a Gabor texture feature of the benign granuloma.

[0019] Example methods and apparatus may also employ 3-fold cross validation where $N=46$ for training a classifier and $N=16$ for testing a classifier. Example methods and apparatus may train a classifier or test a classifier with other, different numbers of subjects. For example, a human pathologist may manually delineate and classify one hundred GGO nodules for a training set and thirty nodules for a testing set. Example methods and apparatus may classify the GGO nodule image as a carcinoma, adenocarcinoma, or as a granuloma. Example methods and apparatus may also classify the GGO nodule image as non-invasive, minimally invasive, or frank invasive. Other classifications may be employed.

[0020] Example methods and apparatus thus improve on conventional methods by more accurately distinguishing between pathological and benign lung nodules.

[0021] Example methods and apparatus distinguish granuloma from carcinoma with an accuracy of at least 92% area under the curve (AUC) when using texture features and shape features with a linear discriminant analysis (LDA) classifier. Example methods and apparatus distinguish frank invasive GGO nodules from non-invasive or minimally invasive GGO

nodules with an accuracy of at least 78% AUC when using three texture features selected by PCA with a quadratic discriminant analysis (QDA) classifier. In contrast, conventional approaches using just Laws feature achieve accuracies of approximately 0.61 AUC, while conventional approaches using just Gabor features achieve accuracies of approximately 0.68 AUC. In these examples, a minimally invasive GGO nodule is defined as a GGO nodule with 5 mm or less invasion, and a frank invasive GGO nodule is defined as a GGO nodule with more than 5 mm invasion. In other embodiments, minimally invasive GGO nodules and frank invasive GGO nodules may be defined on other dimensions.

[0022] By increasing the accuracy with which malignant GGO nodules are distinguished from benign lung GGO nodules, example methods and apparatus produce the concrete, real-world technical effect of reducing the time required to evaluate medical imagery while increasing the accuracy of the evaluation. Additionally, example apparatus and methods increase the probability that at-risk patients receive timely treatment tailored to the particular pathology they exhibit. Example methods and apparatus may also reduce the number of invasive procedures needed to accurately characterize GGO nodules. The additional technical effect of reducing the expenditure of resources and time on patients who are less likely to suffer recurrence or disease progression is also achieved. Example methods and apparatus thus improve on conventional methods in a measurable, clinically significant way.

[0023] Some portions of the detailed descriptions that follow are presented in terms of algorithms and symbolic representations of operations on data bits within a memory. These algorithmic descriptions and representations are used by those skilled in the art to convey the substance of their work to others. An algorithm, here and generally, is conceived to be a sequence of operations that produce a result. The operations may include physical manipulations of physical quantities. Usually, though not necessarily, the physical quantities take the form of electrical or magnetic signals capable of being stored, transferred, combined, compared, and otherwise manipulated in a logic, and so on. The physical manipulations create a concrete, tangible, useful, real-world result.

[0024] It has proven convenient at times, principally for reasons of common usage, to refer to these signals as bits, values, elements, symbols, characters, terms, numbers, and so on. It should be borne in mind, however, that these and similar terms are to be associated with the appropriate physical quantities and are merely convenient labels applied to these quantities. Unless specifically stated otherwise, it is appreciated that throughout the description, terms including processing, computing, calculating, determining, and so on, refer to actions and processes of a computer system, logic, processor, or similar electronic device that manipulates and transforms data represented as physical (electronic) quantities.

[0025] Example methods may be better appreciated with reference to flow diagrams. While for purposes of simplicity of explanation, the illustrated methodologies are shown and described as a series of blocks, it is to be appreciated that the methodologies are not limited by the order of the blocks, as some blocks can occur in different orders and/or concurrently with other blocks from that shown and described. Moreover, less than all the illustrated blocks may be required to implement an example methodology. Blocks may be combined or

separated into multiple components. Furthermore, additional and/or alternative methodologies can employ additional, not illustrated blocks.

[0026] FIG. 1 illustrates an example computerized method 100 for characterizing a GGO nodule in a region of lung tissue. Method 100 includes, at 110, accessing an image of a region of lung tissue. Accessing the image may include accessing a CT image of the region of lung tissue. The CT image may be stored, for example, in a computer memory or may be provided across a computer network. In one embodiment, the CT image is a 1 mm to 5 mm thick, no-contrast chest CT image. In another embodiment, other images sizes or other imaging techniques may be employed.

[0027] Method 100 also includes, at 120, delineating a GGO nodule in the image. The GGO nodule may be automatically delineated by distinguishing GGO nodule tissue within the image from the background of the image. The GGO nodule tissue may be automatically distinguished using threshold based segmentation, deformable boundary models, active-appearance models, active shape models, graph based models including Markov random fields (MRF), min-max cut approaches, or other image segmentation approaches.

[0028] Method 100 also includes, at 130, extracting a set of texture features from the image of the GGO nodule. The set of texture features includes a gray-level statistical feature, a steerable Gabor feature, a Haralick feature, a Law feature, a Law-Laplacian feature, a local binary pattern (LBP) feature, inertia, a correlation feature, a difference entropy feature, a contrast inverse moment feature, or a contrast variance feature. In one embodiment, the set of texture features includes at least sixty three texture features. In another embodiment, the set of texture features includes at least one hundred texture features. For example, a set of one hundred texture features may include 13 Haralick features, 4 gray features, 13 gradient features, 19 Gabor features, 1 LBP feature, 25 Law features, or 25 Law-Laplacian features. In other embodiments, other numbers or types of texture features may be extracted.

[0029] Method 100 also includes, at 140, selecting a subset of texture features from the set of texture features. In one embodiment, the subset of texture features is selected by reducing the set of texture features using a PCA. The PCA of the set of texture features selects a subset of texture features from the set of texture features. The subset of texture features achieves a threshold level of discriminability. For example, the PCA may select one energy feature and one Gabor feature that are the most discriminative, based on a particular set of CT images, for distinguishing carcinoma from granuloma. The subset of texture features may include as few as two texture features. The level of discriminability may be user adjustable. For example, in a first clinical situation, a subset of texture features that achieves 0.8 AUC accuracy in distinguishing carcinoma from granuloma may be acceptable. A feature may be considered to have a desirable level of discriminability when the means of two separate classes are more than a threshold distance from each other, and where the variance of a class is less than a threshold distance, in comparison to the distance between the means. In one embodiment, the Fisher criterion, which is the squared difference of the means divided by the sum of the variances, may be used to quantitatively establish a desirable level of discriminability.

[0030] FIG. 7 is a boxplot of CT intensities of a CT image of a minimally invasive GGO nodule and a frank invasive GGO nodule. In FIG. 7, the Y-axis indicates the normalized value of the average Hounsfield unit within a nodule in the CT

image. FIG. 7 illustrates the challenge involved with classifying GGO nodules using conventional CT imagery approaches. FIG. 7 demonstrates that the CT intensities of a minimally invasive GGO nodule and frank invasive GGO nodule overlap significantly. In this example, the median of the CT intensity for the minimally invasive GGO nodule is within a threshold distance from the median of the frank invasive GGO. Thus, an attempt to classify a GGO nodule based on just CT intensity is unlikely to be acceptably accurate.

[0031] FIG. 8 is a boxplot of CT contrast variance of a CT image of a minimally invasive GGO nodule and a frank invasive GGO nodule. In FIG. 8, the Y-axis indicates the normalized value of the average Hounsfield unit with a nodule in the CT image. FIG. 8 demonstrates how texture features, like contrast variance, may have a more desirable level of discriminability. In this example, the median of the CT contrast variance for the minimally invasive GGO nodule is more than a threshold distance from the median of the CT contrast variance for the frank invasive GGO.

[0032] Method 100 also includes, at 150, generating a phenotypic signature for the nodule. In one embodiment, the phenotypic signature is generated using Fisher criteria ranking. In another embodiment, the phenotypic signature is generated using other techniques.

[0033] Method 100 also includes, at 160, controlling a computer aided diagnosis (CADx) system to generate a classification of the GGO nodule in the image. The classification may be based, at least in part, on the subset of texture features or the phenotypic signature. In one embodiment, the CADx system generates the classification of the image of the GGO nodule using a QDA classifier. In another embodiment, the CADx system may generate the classification using other, different types of classifier. The classifier may be trained and tested on a set of images of pre-classified GGO nodules. In one embodiment, the image is of a region of tissue demonstrating adenocarcinoma pathology. Controlling the CADx system to generate the classification of the GGO nodule based, at least in part, on the subset of texture features and the phenotypic signature, includes classifying the image of the GGO nodule as frank invasive adenocarcinoma or minimally invasive adenocarcinoma.

[0034] Example methods and apparatus facilitate more accurate characterization of GGO nodules found in CT images than conventional approaches. Example methods and apparatus thus improve on conventional methods by characterizing GGO nodules as frank invasive, non-invasive, or minimally invasive, or as carcinomas, adenocarcinomas, or granulomas with greater accuracy and with less subjective variability than conventional methods. Example methods and apparatus therefore facilitate more judicious application of biopsies and surgical resection in a population undergoing CT screening for lung cancer.

[0035] Using a more appropriately determined and applied treatment may lead to less therapeutics being required for a patient or may lead to avoiding or delaying a biopsy, a resection, or other invasive procedure. When regions of cancerous tissue, including GGO nodules detected in CT scans, are more quickly and more accurately classified, patients with poorer prognoses may receive a higher proportion of scarce resources (e.g., therapeutics, physician time and attention, hospital beds) while those with better prognoses may be spared unnecessary treatment, which in turn spares unnecessary expenditures and resource consumption. Example meth-

ods and apparatus may thus have the real-world, quantifiable effect of improving patient outcomes.

[0036] While FIG. 1 illustrates various actions occurring in serial, it is to be appreciated that various actions illustrated in FIG. 1 could occur substantially in parallel. By way of illustration, a first process could delineate a GGO nodule in a CT image, a second process could extract texture features from the CT image, and a third process could extract shape features from the CT image. While three processes are described, it is to be appreciated that a greater or lesser number of processes could be employed and that lightweight processes, regular processes, threads, and other approaches could be employed.

[0037] FIG. 2 illustrates an example method 200 for characterizing a GGO nodule in a region of lung tissue. Method 200 is similar to method 100 but includes additional actions. Method 200 includes actions 210, 220, 230, 240, and 250 which are similar to actions 110, 120, 130, 140, and 150 described above with respect to method 100.

[0038] Method 200 also includes, at 260, extracting a set of shape features from the image of the GGO nodule. The set of shape features includes a location feature, a size feature, a width feature, a height feature, a depth feature, a perimeter feature, an eccentricity feature, an eccentricity standard deviation, a compactness feature, a roughness feature, an elongation feature, a convexity feature, an extend feature, an equivalent diameter feature, or a sphericity feature. The location feature describes the spatial information of a pixel in the image of the GGO nodule, the size feature describes the number of pixels within the segmented image of the GGO nodule, and the perimeter feature describes the distance around the boundary of the segmented GGO nodule. The eccentricity feature describes the eccentricity of an ellipse that has the same second moments as the nodule. The compactness feature describes the isoperimetric quotient of the nodule. The roughness feature describes the perimeter of a lesion in a slice of the image of the GGO nodule divided by the convex perimeter of the lesion. The elongation feature describes the ratio of minor axis to the major axis of the image of the GGO nodule, and the convexity feature describes the ratio of a tumor image slice to the convex hull of the tumor. The extend feature describes the ratio of pixels in the tumor region to pixels in the total bounding box. The equivalent diameter feature describes the diameter of a circle having the same area as a tumor image slice, and the sphericity feature describes the three-dimensional compactness of the nodule. In one embodiment the set of shape features includes at least twenty-five shape features. In another embodiment, the set of shape features may include other numbers of shape features, or other, different shape features. A feature may be calculated in three dimensional (3D) space, or in two dimensional (2D) space. For example, width, height, depth, or sphericity features may be calculated in 3D space.

[0039] Method 200 also includes, at 270, selecting a subset of shape features from the set of shape features. In one embodiment, the subset of shape features includes eccentricity, eccentricity standard deviation, or elongation features. In another embodiment, the subset of shape features may include other, different shape features. The subset of shape features may be selected from the set of shape features using PCA.

[0040] Method 200 also includes, at 280, controlling the CADx system to generate the classification of the image of the GGO nodule as a carcinoma or a granuloma. The classification may be based, at least in part, on the subset of texture

features and the subset of shape features. Basing the classification on both the subset of texture features and the subset of shape features improves on conventional approaches by equivalent diameter feature, or a sphericity feature. The location feature describes the spatial information of a pixel in the image of the GGO nodule, the size feature describes the number of pixels within the segmented image of the GGO nodule, and the perimeter feature describes the distance around the boundary of the segmented GGO nodule. The eccentricity feature describes the eccentricity of an ellipse that has the same second moments as the nodule. The compactness feature describes the isoperimetric quotient of the nodule. The roughness feature describes the perimeter of a lesion in a slice of the image of the GGO nodule divided by the convex perimeter of the lesion. The elongation feature describes the ratio of minor axis to the major axis of the image of the GGO nodule, and the convexity feature describes the ratio of a tumor image slice to the convex hull of the tumor. The extend feature describes the ratio of pixels in the tumor region to pixels in the total bounding box. The equivalent diameter feature describes the diameter of a circle having the same area as a tumor image slice, and the sphericity feature describes the three-dimensional compactness of the nodule. In one embodiment the set of shape features includes at least twenty-five shape features. In another embodiment, the set of shape features may include other numbers of shape features, or other, different shape features. A feature may be calculated in three dimensional (3D) space, or in two dimensional (2D) space. For example, width, height, depth, or sphericity features may be calculated in 3D space.

[0041] Method 200 also includes, at 270, selecting a subset of shape features from the set of shape features. In one embodiment, the subset of shape features includes eccentricity, eccentricity standard deviation, or elongation features. In another embodiment, the subset of shape features may include other, different shape features. The subset of shape features may be selected from the set of shape features using PCA.

[0042] Method 200 also includes, at 280, controlling the CADx system to generate the classification of the image of the GGO nodule as a carcinoma or a granuloma. The classification may be based, at least in part, on the subset of texture features and the subset of shape features. Basing the classification on both the subset of texture features and the subset of shape features improves on conventional approaches by increasing the accuracy with which the image of the GGO may be classified. In one embodiment, the CADx system generates the classification of the image of the GGO nodule using a LDA classifier or a QDA classifier. In one embodiment, an LDA classifier using a median textural feature and eccentricity standard deviation shape feature achieves an accuracy of at least 0.92 AUC. The LDA classifier or the QDA classifier may be trained and tested on a set of GGO images pre-classified as carcinoma or granuloma.

[0043] In one embodiment, method 200 may also automatically segment vessels associated with the nodule. Method 200 may identify a centerline of a vessel and branching points associated with the vessel. Method 200 calculates the torsion for a vessel segment using a distance metric. The torsion of a vessel segment is defined as $1 - (\text{Distance}/\text{Length})$ where distance is the Euclidean distance of the start and end point of the segment, and where length is the number of voxels along the vessel segment. Method 200 also extracts the curvature of a vessel segment. Curvature at a voxel of a vessel segment is

proportional to the inverse of an osculating circle's radius. The osculating circle is fitted to a collection of three neighboring points along the centerline of a vessel. For a plurality of points along the center line of a vessel, method 200 fits a circle to compute the curvature of a specific point. Method 200 then computes mean and standard deviation of the curvature for points along the vessel.

[0044] Method 200 may then extract a set of tortuosity features from the image of the GGO nodule. The tortuosity features describe vessels associated with the GGO nodule. The set of tortuosity features includes the mean of torsion of a vessel segment, or the standard deviation of torsion of a vessel segment. The set of tortuosity features also includes the mean and standard deviation of the mean curvature of a group of vessel segments. The set of tortuosity features also includes the mean and standard deviation of the standard deviation of a vessel segment curvature and a total vessel segment length. In one embodiment, the set of tortuosity features includes at least seven tortuosity features. In another embodiment, the set of tortuosity features may include other numbers of tortuosity features, or other, different tortuosity features. Method 200 may also select of subset of tortuosity features from the set of tortuosity features. Method 200 may also include controlling the CADx system to generate the classification of the image of the GGO nodule based, at least in part, on the subset of tortuosity features, the subset of texture features and the subset of shape features.

[0045] FIG. 3 illustrates an example method 300 for distinguishing invasive tumors from non-invasive tumors in chest CT images. Method 300 includes, at 310 accessing an image of a region of tissue demonstrating cancerous pathology. In one embodiment, the image is a 1 mm to 5 mm thick, no-contrast chest CT image. In another embodiment, other image types or image dimensions may be used. Accessing the image may include retrieving electronic data from a computer memory, receiving a computer file over a computer network, or other computer or electronic based action.

[0046] Method 300 also includes, at 320, segmenting a tumor in the image from the background of the image. Segmenting the tumor in the image from the background of the image involves identifying the portion of the image that represents the tumor to distinguish that portion from the background. In one embodiment, the tumor is automatically segmented from the background of the image. In another embodiment, a human pathologist manually delineates the tumor from the background of the image. In another embodiment, vessels associated with the tumor are also segmented.

[0047] Method 300 also includes, at 330, selecting a set of texture features from the segmented image. In one embodiment, the set of texture features may include a gray-level statistical feature, a steerable Gabor feature, a Haralick feature, a Law feature, a Law-Laplacian feature, an LBP feature, an inertia feature, a correlation feature, a difference entropy feature, a contrast inverse moment feature, or a contrast variance feature. In another embodiment, other, different texture features may be selected. The inertia feature describes the contrast or local intensity variation of the segmented image. The correlation feature describes the correlation of the intensity of values within the segmented image. The difference entropy feature describes the disorder of the difference between a pair of pixel intensities within the segmented image. The contrast inverse moment feature describes the inhomogeneity within a region of interest in the segmented

image. The contrast variance feature describes the variance of the difference between a pair of pixel intensities.

[0048] Method 300 also includes, at 340, selecting a set of shape features from the segmented image. The set of shape features may include a location feature, a size feature, a perimeter feature, an eccentricity feature, an eccentricity standard deviation, a compactness feature, a roughness feature, an elongation feature, a convexity feature, an equivalent diameter feature, a radial distance feature, an area feature, or a sphericity feature. The radial distance feature describes the radial distance from the center of mass of the tumor to a point on the defining contour of the tumor.

[0049] Method 300 also includes, at 345, selecting a set of tortuosity features from the segmented image. The set of tortuosity features may include the mean of torsion of a vessel segment, or the standard deviation of torsion of a vessel segment. The set of tortuosity features may also include the mean and standard deviation of the mean curvature of a group of vessel segments. The set of tortuosity features may also include the mean and standard deviation of the standard deviation of a vessel segment curvature and a total vessel segment length. In one embodiment, the set of tortuosity features includes at least seven tortuosity features. In another embodiment, the set of tortuosity features may include other numbers of tortuosity features, or other, different tortuosity features.

[0050] Method 300 also includes, at 350, generating a classification for the tumor based, at least in part, on the set of texture features, the set of shape features, and the set of tortuosity features. In one embodiment, the classification is made based on the set of texture features. In another embodiment, the classification is based on the set of shape features. In still another embodiment, the classification is based on a subset of the set of texture features, a subset of the set of shape features, and a subset of the set of tortuosity features. The subset of the set of texture features may be selected from the set of texture features using PCA. The subset of the set of shape features may be selected from the set of shape features using PCA. The subset of the set of tortuosity features may be selected from the set of tortuosity features using PCA. The subset of shape features, the subset of texture features, or the subset of tortuosity features may be selected to achieve a threshold level of accuracy when classifying tumors. In one embodiment, method 300 classifies the tumor as a carcinoma or a granuloma. In another embodiment, the tumor is classified as frank invasive, minimally invasive, or non-invasive. The classification may be made by a CADx system using a QDA classifier or an LDA classifier.

[0051] Method 300 also includes, at 360, providing a prognosis prediction based on the classification. For example, method 300 may, at 360, provide a probability that a patient will experience a lower five year survival rate if the tumor is classified as frank invasive. Method 300 may alternately provide a probability that a patient will experience a higher five year survival rate if the tumor is classified as non-invasive.

[0052] In one example, a method may be implemented as computer executable instructions. Thus, in one example, a computer-readable storage medium may store computer executable instructions that if executed by a machine (e.g., computer) cause the machine to perform methods described or claimed herein including method 100, method 200, and method 300. While executable instructions associated with the listed methods are described as being stored on a computer-readable storage medium, it is to be appreciated that

executable instructions associated with other example methods described or claimed herein may also be stored on a computer-readable storage medium. In different embodiments the example methods described herein may be triggered in different ways. In one embodiment, a method may be triggered manually by a user. In another example, a method may be triggered automatically.

[0053] FIG. 4 illustrates an example apparatus 400 for classifying a region of tissue in an image. Apparatus 400 includes a processor 410, a memory 420, a set of logics 440, and an interface 430 that connects the processor 410, the memory 420, and the set of logics 440. The set of logics 440 includes an image acquisition logic 441, a delineation logic 443, a texture logic 445, a phenotype signature logic 446, a shape logic 447, and a classification logic 449. In one embodiment, the functionality associated with the set of logics 440 may be performed, at least in part, by hardware logic components including, but not limited to, field-programmable gate arrays (FPGAs), application specific integrated circuits (ASICs), application specific standard products (ASSPs), system on a chip systems (SOCs), or complex programmable logic devices (CPLDs). In one embodiment, individual members of the set of logics 440 are implemented as ASICs or SOCs.

[0054] Image acquisition logic 441 acquires an image of a region of tissue. The image may be acquired from, for example, a CT apparatus. The region of tissue may be a section of tissue demonstrating cancerous pathology in a patient. The image of the region of tissue may include an image of a GGO nodule. In one embodiment, the image is a 1 mm to 5 mm thick, no-contrast chest CT image. Other imaging approaches may be used to generate and access the image accessed by image acquisition logic 441. Other image dimensions may also be used.

[0055] Delineation logic 443 automatically delineates the GGO nodule by distinguishing GGO nodule tissue within the image from the background of the image. Delineation logic 443 automatically delineates the GGO nodule using threshold based segmentation, deformable boundary models, active-appearance models, active shape models, graph based models including Markov random fields (MRF), min-max cut approaches, or other image segmentation approaches.

[0056] Texture logic 445 extracts a set of texture features from the image. The set of texture features may be extracted from the image of the delineated GGO nodule. In one embodiment, the set of texture features includes a gray-level statistical feature, a steerable Gabor feature, a Haralick feature, a Law feature, a Law-Laplacian feature, an LBP feature, inertia, correlation, difference entropy, contrast inverse moment, or contrast variance. The texture logic 445 may also select a subset of texture features from the set of texture features. Texture logic 445 may select the subset of texture features based on, at least in part, a PCA of the set of texture features.

[0057] Phenotype selection logic 446 computes a phenotypic signature of the delineated GGO nodule in the image. Phenotype selection logic 446 may compute the phenotypic signature using a Fisher criteria ranking.

[0058] Shape logic 447 extracts a set of shape features from the image. The set of shape features may include a location feature, a size feature, a perimeter feature, an eccentricity feature, an eccentricity standard deviation, a compactness feature, a roughness feature, an elongation feature, a convexity feature, an equivalent diameter feature, or a sphericity

feature. Shape logic 447 also selects a subset of shape features from the set of shape features based, at least in part, on a PCA of the set of shape features.

[0059] Classification logic 449 classifies the GGO nodule tissue based, at least in part, on the set of texture features, the phenotypic signature, or the set of shape features. In one embodiment, classification logic 449 logic classifies the GGO nodule tissue as a carcinoma or a granuloma using an LDA of the subset of texture features and the subset of shape features. In another embodiment, classification logic 449 classifies the GGO nodule tissue as minimally invasive or as frank invasive using a QDA of the subset of texture features. In still another embodiment, classification logic 449 may classify the GGO nodule tissue using other analytical techniques.

[0060] In another embodiment, classification logic 449 may control a CADx system to classify the image based, at least in part, on the classification. For example, classification logic 449 may control a lung cancer CADx system to classify the image based, at least in part, on the set of texture features and set of shape features. In other embodiments, other types of CADx systems may be controlled, including CADx systems for distinguishing GGO nodules among oral cancer, prostate cancer, colon cancer, brain cancer, and other diseases where disease classification and prognosis prediction may be based on textural or shape features quantified from CT images of a GGO nodule.

[0061] In one embodiment of apparatus 400, the set of logics 440 also includes a tortuosity logic. The tortuosity logic identifies a vessel associated with the GGO nodule. The tortuosity logic identifies the centerline and a branching point of the vessel associated with the GGO nodule. The tortuosity logic computes a torsion for the segment of the vessel. The tortuosity logic also computes a curvature of a voxel of a vessel segment, where the curvature is proportional to the inverse of an osculating circle's radius. The tortuosity logic extracts a set of tortuosity features from the image. The set of tortuosity features may include the mean of torsion of a vessel segment, or the standard deviation of torsion of a vessel segment. The set of tortuosity features also may include the mean and standard deviation of the mean curvature of a group of vessel segments. The set of tortuosity features also may include the mean and standard deviation of the standard deviation of a vessel segment curvature and a total vessel segment length. The tortuosity logic also selects a subset of tortuosity features from the set of tortuosity features based, at least in part, on a PCA of the set of tortuosity features. The subset of tortuosity features may include at least three tortuosity features. In this embodiment, the classification logic 449 classifies the GGO nodule tissue based, at least in part, on the set of tortuosity features, the set of texture features, the phenotypic signature, or the set of shape features.

[0062] In one embodiment of apparatus 400, the set of logics 440 also includes a display logic. The display logic may control the CADx system to display the classification, the texture features, or the shape features on a computer monitor, a smartphone display, a tablet display, or other displays. Displaying the classification or the features may also include printing the classification or the features. The display logic may also control the CADx to display an image of the region of tissue demonstrating a GGO nodule. The image of the region of tissue demonstrating a GGO nodule may include a delineated or segmented representation of the GGO nodule. By displaying the features and the image of the GGO nodule,

example apparatus provide a timely and intuitive way for a human pathologist to more accurately classify pathologies demonstrated by a patient, thus improving on conventional approaches to predicting cancer recurrence and disease progression.

[0063] FIG. 5 illustrates an example computer 500 in which example methods illustrated herein can operate and in which example logics may be implemented. In different examples, computer 500 may be part of a CT system, may be operably connectable to a CT system, or may be part of a CADx system.

[0064] Computer 500 includes a processor 502, a memory 504, and input/output ports 510 operably connected by a bus 508. In one example, computer 500 may include a set of logics 530 that perform a method of characterizing a GGO nodule in a region of lung tissue. Thus, the set of logics 530, whether implemented in computer 500 as hardware, firmware, software, and/or a combination thereof may provide means (e.g., hardware, software) for characterizing a GGO nodule in a region of lung tissue. In different examples, the set of logics 530 may be permanently and/or removably attached to computer 500. In one embodiment, the functionality associated with the set of logics 530 may be performed, at least in part, by hardware logic components including, but not limited to, field-programmable gate arrays (FPGAs), application specific integrated circuits (ASICs), application specific standard products (ASSPs), system on a chip systems (SOCs), or complex programmable logic devices (CPLDs). In one embodiment, individual members of the set of logics 530 are implemented as ASICs or SOCs.

[0065] Processor 502 can be a variety of various processors including dual microprocessor and other multi-processor architectures. Memory 504 can include volatile memory and/or non-volatile memory. A disk 506 may be operably connected to computer 500 via, for example, an input/output interface (e.g., card, device) 518 and an input/output port 510. Disk 506 may include, but is not limited to, devices like a magnetic disk drive, a tape drive, a Zip drive, a flash memory card, or a memory stick. Furthermore, disk 506 may include optical drives like a CD-ROM or a digital video ROM drive (DVD ROM). Memory 504 can store processes 514 or data 517, for example. Disk 506 or memory 504 can store an operating system that controls and allocates resources of computer 500.

[0066] Bus 508 can be a single internal bus interconnect architecture or other bus or mesh architectures. While a single bus is illustrated, it is to be appreciated that computer 500 may communicate with various devices, logics, and peripherals using other busses that are not illustrated (e.g., PCIe, SATA, Infiniband, 1394, USB, Ethernet).

[0067] Computer 500 may interact with input/output devices via I/O interfaces 518 and input/output ports 510. Input/output devices can include, but are not limited to, digital whole slide scanners, an optical microscope, a keyboard, a microphone, a pointing and selection device, cameras, video cards, displays, disk 506, network devices 520, or other devices. Input/output ports 510 can include but are not limited to, serial ports, parallel ports, or USB ports.

[0068] Computer 500 may operate in a network environment and thus may be connected to network devices 520 via I/O interfaces 518 or I/O ports 510. Through the network devices 520, computer 500 may interact with a network. Through the network, computer 500 may be logically connected to remote computers. The networks with which com-

puter 500 may interact include, but are not limited to, a local area network (LAN), a wide area network (WAN), or other networks.

[0069] References to “one embodiment”, “an embodiment”, “one example”, and “an example” indicate that the embodiment(s) or example(s) so described may include a particular feature, structure, characteristic, property, element, or limitation, but that not every embodiment or example necessarily includes that particular feature, structure, characteristic, property, element or limitation. Furthermore, repeated use of the phrase “in one embodiment” does not necessarily refer to the same embodiment, though it may.

[0070] “Computer-readable storage medium”, as used herein, refers to a medium that stores instructions or data. “Computer-readable storage medium” does not refer to propagated signals. A computer-readable storage medium may take forms, including, but not limited to, non-volatile media, and volatile media. Non-volatile media may include, for example, optical disks, magnetic disks, tapes, and other media. Volatile media may include, for example, semiconductor memories, dynamic memory, and other media. Common forms of a computer-readable storage medium may include, but are not limited to, a floppy disk, a flexible disk, a hard disk, a magnetic tape, other magnetic medium, an application specific integrated circuit (ASIC), a compact disk (CD), other optical medium, a random access memory (RAM), a read only memory (ROM), a memory chip or card, a memory stick, and other media from which a computer, a processor or other electronic device can read.

[0071] “Logic”, as used herein, includes but is not limited to hardware, firmware, software in execution on a machine, or combinations of each to perform a function(s) or an action(s), or to cause a function or action from another logic, method, or system. Logic may include a software controlled microprocessor, a discrete logic (e.g., ASIC), an analog circuit, a digital circuit, a programmed logic device, a memory device containing instructions, and other physical devices. Logic may include one or more gates, combinations of gates, or other circuit components. Where multiple logical logics are described, it may be possible to incorporate the multiple logical logics into one physical logic. Similarly, where a single logical logic is described, it may be possible to distribute that single logical logic between multiple physical logics.

[0072] To the extent that the term “includes” or “including” is employed in the detailed description or the claims, it is intended to be inclusive in a manner similar to the term “comprising” as that term is interpreted when employed as a transitional word in a claim.

[0073] Throughout this specification and the claims that follow, unless the context requires otherwise, the words ‘comprise’ and ‘include’ and variations such as ‘comprising’ and ‘including’ will be understood to be terms of inclusion and not exclusion. For example, when such terms are used to refer to a stated integer or group of integers, such terms do not imply the exclusion of any other integer or group of integers.

[0074] To the extent that the term “or” is employed in the detailed description or claims (e.g., A or B) it is intended to mean “A or B or both”. When the applicants intend to indicate “only A or B but not both” then the term “only A or B but not both” will be employed. Thus, use of the term “or” herein is the inclusive, and not the exclusive use. See, Bryan A. Garner, *A Dictionary of Modern Legal Usage* 624 (2d. Ed. 1995).

[0075] While example systems, methods, and other embodiments have been illustrated by describing examples,

and while the examples have been described in considerable detail, it is not the intention of the applicants to restrict or in any way limit the scope of the appended claims to such detail. It is, of course, not possible to describe every conceivable combination of components or methodologies for purposes of describing the systems, methods, and other embodiments described herein. Therefore, the invention is not limited to the specific details, the representative apparatus, and illustrative examples shown and described. Thus, this application is intended to embrace alterations, modifications, and variations that fall within the scope of the appended claims.

What is claimed is:

1. A non-transitory computer-readable storage medium storing computer executable instructions that when executed by a computer control the computer to perform a method for characterizing a ground glass (GGO) nodule in a region of lung tissue, the method comprising:

accessing an image of a region of lung tissue; delineating a GGO nodule in the image; extracting a set of texture features from the GGO nodule; selecting a subset of texture features from the set of texture features; extracting a set of shape features from the GGO nodule; selecting a subset of shape features from the set of shape features; generating a phenotypic signature for the nodule; and controlling a computer aided diagnosis (CADx) system to generate a classification of the GGO nodule in the image based, at least in part, on the subset of texture features, the subset of shape features, or the phenotypic signature.

2. The non-transitory computer-readable storage medium of claim **1**, where accessing the image of the region of lung tissue includes accessing a computed tomography (CT) image of the region of lung tissue, where the CT image is a no-contrast chest CT image.

3. The non-transitory computer-readable storage medium of claim **1**, the method comprising automatically delineating the GGO nodule by distinguishing GGO nodule tissue in the image from the background of the image.

4. The non-transitory computer-readable storage medium of claim **1**, where the set of texture features includes at least sixty three texture features.

5. The non-transitory computer-readable storage medium of claim **1**, where the set of texture features includes a gray-level statistical feature, a steerable Gabor feature, a Haralick feature, a Law feature, a Law-Laplacian feature, an LBP feature, an inertia feature, a correlation feature, a difference entropy feature, a contrast inverse moment feature, a gradient feature, or a contrast variance feature.

6. The non-transitory computer-readable storage medium of claim **1**, where selecting the subset of texture features from the set of texture features includes reducing the set of texture features using principal component analysis (PCA).

7. The non-transitory computer-readable storage medium of claim **1**, where the phenotypic signature is generated using Fisher criteria ranking.

8. The non-transitory computer-readable storage medium of claim **1**, where the CADx system generates the classification of the image of the GGO nodule using a quadratic discriminant analysis (QDA) classifier.

9. The non-transitory computer-readable storage medium of claim **1**, where the image is of a region of adenocarcinoma tissue, and where controlling the CADx system to generate the classification of the image of the GGO nodule based, at

least in part, on the subset of texture features and the phenotypic signature, includes classifying the image of the GGO nodule as frank invasive adenocarcinoma or minimally invasive adenocarcinoma.

10. The non-transitory computer-readable storage medium of claim **1**, where the set of shape features includes a location feature, a size feature, a width feature, a height feature, a depth feature, a radial distance feature, a perimeter feature, an eccentricity feature, an eccentricity standard deviation, a compactness feature, a roughness feature, an elongation feature, a convexity feature, an equivalent diameter feature, or a sphericity feature.

11. The non-transitory computer-readable storage medium of claim **10**, where the subset of shape features includes an eccentricity feature, an eccentricity standard deviation feature, or an elongation feature.

12. The non-transitory computer-readable storage medium of claim **11**, the method comprising controlling the CADx system to generate the classification of the image of the GGO nodule as a carcinoma or a granuloma based, at least in part, on the subset of texture features and the subset of shape features.

13. The non-transitory computer-readable storage medium of claim **12**, the method further comprising:

segmenting a vessel associated with the image of the GGO nodule into a plurality of vessel segments; computing a torsion for a vessel segment; computing a curvature for the vessel segment, where the curvature is proportional to the inverse of the radius of an osculating circle;

selecting a set of tortuosity features from the image of the GGO nodule, where the set of tortuosity features includes a mean of torsion of the vessel segment, a standard deviation of torsion of the vessel segment, a mean of the mean curvature of the plurality of vessel segments, a standard deviation of the mean curvature of the plurality of vessel segments, a mean of the standard deviation of the curvature of the vessel segment, a standard deviation of the standard deviation of the curvature of the vessel segment, a total length of a vessel segment, or a total length of the plurality of vessel segments;

selecting a subset of tortuosity features from the set of tortuosity features using a PCA of the set of tortuosity features; and

controlling a computer aided diagnosis (CADx) system to generate a classification of the GGO nodule in the image based, at least in part, on the subset of tortuosity features, the subset of texture features, the subset of shape features, or the phenotypic signature.

14. The non-transitory computer-readable storage medium of claim **1**, where the CADx system generates the classification of the image of the GGO nodule using a linear discriminant analysis (LDA) classifier or a quadratic discriminant analysis (QDA) classifier.

15. The non-transitory computer-readable storage medium of claim **14**, where the LDA classifier classifies the image of the GGO nodule with an accuracy of at least 0.92 area under the curve (AUC).

16. A method for distinguishing tumors in a medical image, the method comprising:

accessing an image of a region of tissue demonstrating cancerous pathology; segmenting a tumor in the image from the background of the image;

selecting a set of texture features from the segmented image;
 selecting a set of shape features from the segmented image;
 generating a classification for the tumor based, at least in part, on the set of texture features and the set of shape features; and
 providing a prognosis prediction based on the classification.

17. An apparatus for classifying a region of tissue in an image, comprising:
 a processor;
 a memory;
 an input/output interface;
 a set of logics; and
 an interface to connect the processor, the memory, the input/output interface and the set of logics, where the set of logics includes:
 an image acquisition logic that acquires an image of a region of tissue demonstrating ground glass (GGO) nodule pathology;
 a delineation logic that distinguishes GGO nodule tissue in the image from the background of the image;
 a texture logic that extracts a set of texture features from the image;
 a phenotype signature logic that computes a phenotypic signature from the image;
 a shape logic that extracts a set of shape features from the image; and
 a classification logic that classifies the GGO nodule tissue based, at least in part, on the set of texture features, the phenotypic signature, or the set of shape features.

18. The apparatus of claim **17**, where the set of texture features includes a gray-level statistical feature, a steerable Gabor feature, a Haralick feature, a Law feature, a Law-Laplacian feature, a gradient feature, a local binary pattern (LBP) feature, an inertia feature, a correlation feature, a difference entropy feature, a contrast inverse moment feature, or a contrast variance feature, and where the texture logic selects

a subset of texture features from the set of texture features based on, at least in part, a principal component analysis (PCA) of the set of texture features.

19. The apparatus of claim **18**, where the set of shape features includes a location feature, a size feature, a width feature, a height feature, a depth feature, a radial distance feature, a perimeter feature, an eccentricity feature, an eccentricity standard deviation feature, a compactness feature, a roughness feature, an elongation feature, a convexity feature, an equivalent diameter feature, or a sphericity feature, and where the shape logic selects a subset of shape features from the set of shape features based on, at least in part, a PCA of the set of shape features.

20. The apparatus of claim **19**,

where the classification logic classifies the GGO nodule tissue as a carcinoma or a granuloma using a linear discriminant analysis of the subset of texture features and the subset of shape features, or

where the classification logic classifies the GGO nodule tissue as minimally invasive or as frank invasive using a quadratic discriminant analysis of the subset of texture features.

21. The apparatus of claim **20**, the set of logics comprising a tortuosity logic that extracts a set of tortuosity features from the image, the set of tortuosity features including a mean of torsion of the vessel segment, the standard deviation of torsion of the vessel segment, a mean of the mean curvature of the plurality of vessel segments, a standard deviation of the mean curvature of the plurality of vessel segments, a mean of the standard deviation of the curvature of the vessel segment, a standard deviation of the standard deviation of the curvature of the vessel segment, a total length of a vessel segment, or a total length of the plurality of vessel segments.

22. The apparatus of claim **21**, where the classification logic classifies the GGO nodule tissue based, at least in part, on the set of tortuosity features, the set of texture features, the phenotypic signature, or the set of shape features.

* * * * *